January 2014

Scanning Tunneling Microscopy And Spectroscopy Studies Of Zinc-Phthalocyanine Adsorption On SiC(0001) And Iridium-Modified Silicon Surfaces

Dylan Nicholls

SCANNING TUNNELING MICROSCOPY AND SPECTROSCOPY STUDIES OF ZINC-PHTHALOCYANINE ADSORPTION ON SIC(0001) AND IRIDIUM-MODIFIED SILICON SURFACES

by

Dylan Nicholls
Bachelor of Science, University of Wisconsin – Eau Claire, 2009

A Dissertation

Submitted to the Graduate Faculty

of the

University of North Dakota

in partial fulfillment of the requirements

for the degree of

Doctor of Philosophy

Grand Forks, North Dakota
May
2014

This dissertation, submitted by Dylan Nicholls in partial fulfillment of the requirements for the Degree of Doctor of Philosophy from the University of North Dakota, has been read by the Faculty Advisory Committee under whom the work has been done and is hereby approved.

_____
Dr. Nuri Oncel

_____
Dr. Ju Kim

_____
Dr. William Schwalm

_____
Dr. Kanishka Marasinghe

_____
Dr. Mark Hoffmann

This dissertation is being submitted by the appointed advisory committee as having met all of the requirements of the School of Graduate Studies at the University of North Dakota and is hereby approved.

_____
Wayne Swisher
Dean of the School of Graduate Studies

_____
Date

PERMISSION

Title Scanning Tunneling Microscopy and Spectroscopy Studies of Zinc-Phthalocyanine Adsorption on SiC(0001) and Iridium-Modified Silicon Surfaces

Department Physics and Astrophysics

Degree Doctor of Philosophy

In presenting this dissertation in partial fulfillment of the requirements for a graduate degree from the University of North Dakota, I agree that the library of this University shall make it freely available for inspection. I further agree that permission for extensive copying for scholarly purposes may be granted by the professor who supervised my dissertation work or, in his absence, by the chairperson of the department or the dean of the Graduate School. It is understood that any copying or publication or other use of this dissertation or part thereof for financial gain shall not be allowed without my written permission. It is also understood that due recognition shall be given to me and to the University of North Dakota in any scholarly use which may be made of any material in my dissertation.

Dylan Nicholls
May 2, 2014

TABLE OF CONTENTS

LIST OF FIGURES vii

ACKNOWLEDGEMENTS x

ABSTRACT xi

CHAPTER

I. INTRODUCTION 1

1.1: Porphyrins and Phthalocyanines on HOPG 2

1.2: Graphene 3

1.3: Iridium-Silicon Surfaces 5

II. MEASUREMENT METHODS 7

2.1: UHV System and Components 7

2.2: STM Theory 8

2.3: Low Energy Electron Diffraction 12

2.4: Auger Electron Spectroscopy 14

III. PHYSISORPTION OF MOLECULES ON HOPG 18

3.1: 5-OIA Assisted Growth of Metal-TCPP Domains on HOPG 19

3.2: Experimental 21

3.3: Results & Discussion 21

3.4: Conclusion 28

IV. PHYSISORPTION OF MOLECULES ON EPITAXIAL GRAPHENE 29

4.1: Experimental 32

4.2 Results & Discussion 33

4.3: Conclusion 38

V. IRIDIUM ON SILICON 39

5.1: Experimental-Si(111) 40

5.2: Results and Discussion-Si(111) 41

5.3: Experimental-Si(100) 48

5.4: Results and Discussion-Si(100) 49

5.5 Conclusion 56

VI. CONCLUSION 58

REFERENCES 60

LIST OF FIGURES

FIGURE PAGE

2. 1 (A) UHV SYSTEM SETUP WITH A SAMPLE PREPARATION CHAMBER ON LEFT SIDE AND STM EXCLUSIVELY ON THE RIGHT SIDE. (B) LEED SCREEN AND AUGER CMA SETUP, $90°$ WITH RESPECT TO ONE ANOTHER..... 8

2. 2 ONE-DIMENSIONAL REPRESENTATION OF POTENTIAL BARRIERS. (A) NON-INTERACTING SYSTEM WITH ENERGY E_{VAC}. (B) TIP AND SAMPLE IN EQUILIBRIUM WITH COMMON FERMI ENERGIES AND THE DIFFERENCE BETWEEN WORK FUNCTIONS IS DEPICTED AS AN ELECTRIC FIELD IN THE GAP. (C) AN APPLIED VOLTAGE PROMOTES TUNNELING BETWEEN TIP AND SAMPLE WHERE THE ENERGIES IN THE GRAY AREA CAN CONTRIBUTE TO TUNNELING..... 9

2. 3 (A) SCHEMATIC OF LEED SETUP WITH SAMPLE. (B) EWALD CONSTRUCTION OF SURFACE SCATTERING WHERE DIFFRACTION PATTERN IS THE RODS VERTICAL TO THE SURFACE..... 14

2. 4 SCHEMATIC OF AES SETUP WITH SAMPLE SET AT A GRAZING ANGLE WITH RESPECT TO INCIDENT ELECTRONS. 16

3. 1 SCHEMATICS OF FE-TCPP, CU-TCPP, AND 5-OIA MOLECULES. 20

3. 2 (A) $19.1nm \times 19.1nm$ STM IMAGE OF 5-OIA ON HOPG, $Vtip = 0.88V, I = 0.45nA$. (B) $25.2nm \times 25.2nm$ STM IMAGE OF TWO CU-TCPP MOLECULES (TWO WHITE BLOBS) ADSORBED ON 5-OIA MODIFIED HOPG SURFACE, $Vtip = 1.1V, I = 0.6nA$. 22

3. 3 (A) $29.4nm \times 29.4nm$ STM IMAGE OF CU-TCPP CHAIN OVER 5-OIA HEAD GROUPS, $Vtip = 1.2V, I = 0.7nA$. (B) $30.5nm \times 30.5nm$ STM IMAGE OF CU-TCPP 2-D PATCH BUILDING NEXT TO A STEP EDGE (DENOTED BY SE), $Vtip = 1.2V, I = 0.6nA$. 23

3. 4 (A) $100nm \times 100nm$ STM IMAGE OF FE-TCPP AND 5-OIA DOMAINS, $Vtip = 1.1V, I = 0.4nA$. (B) SCHEMATIC OF FE-TCPP CHAINS OVER THE HEAD GROUPS OF 5-OIA. (C) $30nm \times 30nm$ STM IMAGE OF FE-TCPP HEXAGONAL DOMAIN, $Vtip = 1.1V, I = 0.18nA$. (D) SCHEMATIC OF HEXAGONAL DOMAINS, AGAIN WITH FE-TCPP OVER THE HEAD GROUPS OF 5-OIA. 26

4. 1 (A) TWO-DIMENSIONAL BAND STRUCTURE OF GRAPHENE SHOWING THE DIRAC POINT AT THE K-POINT AND FERMI LEVEL. 30

4. 2 SCHEMATIC OF ZN-PC MOLECULE..... 32

4. 3 (A) SCHEMATIC OF GRAPHENE. (B) SIDE-VIEW SCHEMATIC SHOWING GRAPHENE ATOP THE 63 BUFFER LAYER ON A SIC SUBSTRATE. (C) $10nm \times 3.75nm$ STM IMAGE OF GRAPHENE OVER 63 RECONSTRUCTION. $V = -0.774V, I = 0.827nA$. 34

4. 4 (A) $5nm \times 5nm$ STM IMAGE OF GRAPHENE OVER 63 RECONSTRUCTION $V = -0.606V$, $I = 0.508nA$. (B) $25nm \times 25nm$ STM IMAGE OF ZN-PC MOLECULES ON GRAPHENE $V = -0.929V$, $I = 0.777nA$. (C) $9nm \times 9nm$ STM IMAGE OF HIGHLIGHTED REGION IN (B), $V = -0.929V$, $I = 0.777nA$ AND RESPECTIVE LINE SCANS ACROSS EACH OF THE ZN-PC MOLECULES. 37

4. 5 (A) LDOS COMPARISON OF THE GRAPHENE SURFACE, EDGE OF THE ZN-PC MOLECULE, INNER-CORE OF THE ZN-PC MOLECULE. (B) SECTION OF THE SAME LDOS CURVES IN (A), NEAR THE DIRAC POINT $\sim 0.41eV$. CLEAR SHIFTS OF THE DIRAC POINT NEAR THE (EDGE/INNER-CORE) OF THE ZN-PC MOLECULE ARE EVIDENCE OF (N-DOPING/P-DOPING), RESPECTIVELY. 38

5. 1 (A) 16.75NM $\times$ 16.75NM STM IMAGE OF SI(111)-7×7, $V = -1.709V, I = 0.398nA$. (B) LEED INTENSITY IMAGE OF SAME SURFACE AT $48eV$ 41

5. 2 LEED PATTERN SEQUENCE AFTER ANNEALING AT: (A) $\sim 350℃ - 650℃$ SHOWING ONLY A SI 1×1 PATTERN, (B) $\sim 750℃$ WITH $7 \times 7\ R19.1°$ PATTERN. 42

5. 3 (A) $180nm \times 180nm$ STM IMAGE OF SI(111)-$\sqrt{7} \times \sqrt{7}R19.1°$ RECONSTRUCTED SURFACE, $V = -1.60V, I = 0.42nA$. (B) $18nm \times 18nm$ STM IMAGE OF THE $\sqrt{7} \times \sqrt{7}$ DOMAIN BOUNDARY, CLEARLY SHOWING A ROTATION OF $\theta = 19.1°$, $V = -1.40V, I = 0.32nA$. (C) $25nm \times 25nm$ STM IMAGE OF A LARGE HOLE ON SURFACE WITH THE LINE SCAN PRESENTED IN (D). (E) SCHEMATIC SHOWING IR-RING CLUSTERS ARE ON SAME TERRACE AS SI(111)-7×7. 44

5. 4 (A) $100nm \times 50nm$ STM IMAGE OF IR MODIFIED SI(111) SURFACE AFTER ANNEALING AT $\sim 1250℃$, $V = -1.40V, I = 0.25nA$. (B) $40nm \times 20nm$ STM IMAGE OF SAME SURFACE SHOWING DOMAINS OF IR-SILICIDE RING CLUSTERS, $V = -1.60V, I = 0.25nA$. (C,D) $4.5nm \times 4.5nm$ STM IMAGES TAKEN WITH DUAL VOLTAGE SCAN WITH (C) $V = -1.60V$ AND (D) $V = 1.20V$ AND $I = 0.42nA$ FOR BOTH. THE GREEN CIRCLES INDICATE THE SAME RING CLUSTER AND THE BLUE DOTS IN (D) INDICATE THE CAPPING ADATOMS. (E) SCHEMATIC OF IR-RING CLUSTER WITH BLUE AND RED DOTS REPRESENTING THE CAPPING AND BRIDGING ADATOMS, RESPECTIVELY. 45

5. 5 LDOS CURVES MEASURED ON (A) A CLEAN SI(111)-7×7 SURFACE, (B) $\sqrt{7} \times \sqrt{7}$ DOMAIN, AND (C) '1×1' DOMAIN. 48

5. 6 LEED INTENSITY IMAGES OF: (A) CLEAN SI(100)-2×1 RECONSTRUCTED SURFACE, (B) IR-MODIFIED SI(100) SURFACE WITH A $p(2 \times 2)$ PATTERN, (C,D,E) SURFACE AFTER ANNEALING AT $800℃$, $900℃$, AND $1000℃$, RESPECTIVELY. THE ELECTRON ENERGY FOR ALL LEED IMAGES IS 49EV. 50

5. 7 (A) LEED INTENSITY IMAGE SHOWING SI(100)-2×1 RETURNED AFTER THE IR-MODIFIED SAMPLE WAS ANNEALED AT $1250℃$. THE ELECTRON ENERGY IS 49EV. (B) $75nm \times 75nm$ STM IMAGE OF THE SAMPLE AFTER THE LEED IMAGE WAS TAKEN, $V = -1.75V, I = 0.42nA$. 51

5. 8 (A) $80nm \times 80nm$ STM IMAGE OF THE IR MODIFIED SI SURFACE, $V = -1.55V, I = 0.44nA$. INSET IS THE LEED INTENSITY IMAGE OF SUCH A SURFACE WITH THE ELECTRON ENERGY OF 49EV. (B) $40nm \times 40nm$ STM IMAGE OF THE SAME SURFACE, $V = 1.54V, I = 0.44nA$. (C) $40nm \times 40nm$ STM IMAGE OF THE SAME SURFACE, $V = -1.54V, I = 0.44nA$. (D) LINE SCANS MEASURED OVER THE GREEN AND BLUE ARROWS IN (C). THE GREEN (BLUE) ARROW GOES OVER A BOUNDARY THAT SEPARATES TWO IR-SILICIDE TERRACES ROTATED $90°$ $0°$..... 53

5. 9 (A) LEED INTENSITY IMAGE AFTER $0.125ML$ OF IR DEPOSITION AND ANNEALING AT $700℃$. (B) LINE SCAN OF LEED IMAGE FROM (01) BEAM TO (21) BEAM. THE ELECTRON ENERGY FOR THE LEED PATTERN IS 49EV. INSET IS THE CORRESPONDING LARGE-SCALE STM IMAGE OF THE SURFACE. 54

5. 10 (A) $25nm \times 25nm$ STM IMAGE SHOWING BOTH IR-SILICIDE TERRACE AND SI(100) SURFACE, $V = -1.0V, I = 0.5nA$. (B) $24nm \times 24nm$ STM IMAGE OF THE IR MODIFIED SI(100) SURFACE, $V = -1.0V, I = 0.5nA$. THE LONGER ARROWS INDICATES BOTH THE DIRECTION OF IR-SILICIDE NANOWIRES AND DIMER ROWS OF SI(100). (C) LINE SCAN OVER THE SHORTER ARROW PRESENTED WITH A MODEL OF THE SI(100) TERRACE. 55

5. 11 (A) $4.5nm \times 2nm$ 3-D STM IMAGE OF THE IR-SILICIDE NANOWIRES, $V = -1.0V, I = 0.5nA$. (B) TOP (BOTTOM) SHOWS A LINE SCAN ALONG (ACROSS) THE NANOWIRES. A SCHEMATIC MODEL FOR THE IR-SILICIDE NANOWIRES IS PRESENTED BETWEEN THE LINE SCANS. 56

ACKNOWLEDGEMENTS

I wish to express my sincere appreciation for my research advisor Dr. Nuri Öncel; his fair approach to both life and work has undoubtedly been the reason that I learned and succeeded as much as I have. I also take this opportunity to express my gratitude for how much time and effort that he has spent one-on-one with me to show and teach me everything about solid-state physics research and at times, life in general.

As for my graduate studies, I would like to thank Dr. William A. Schwalm, Dr. Ju Kim, Dr. Kanishka Marasinghe and Dr. Mark Hoffmann for serving in my dissertation committee. I would also like to thank the rest of the Department of Physics faculty for their constant support throughout my graduate studies and Rob Czapiewski for his talents and hard work to help maintain our laboratory equipment.

Finally, I would like to thank Ben Ware for his friendship and vital research contributions to each project in this dissertation.

I would like to dedicate this dissertation to my fiancé Abha Mistry and my ever supportive parents, Diane and Dan Nicholls.

ABSTRACT

Studies were performed on two seemingly different topics, molecular thin films on graphite/graphene and metal induced changes in various cuts of silicon (Si) surfaces. However, both projects share the underlying theme of self-assembly. Since nature can rely upon self-assembly at the nano-scale, all that is needed is to discover functional means to create components for integrated circuits as well as electronic and photonic devices.

Scanning Tunneling Microscopy and Spectroscopy (STM/STS) studies were carried out to characterize the morphology of thin porphyrin films on graphite and the effects of Zn-Phthalocyanine (Zn-Pc) adsorption on the electronic properties of graphene. It was found that the metal atom complex of porphyrin molecules can determine the morphology, intermolecular forces and ability to create thin films on a graphite surface. Zn-Pc adsorption onto graphene shifts the position of the Dirac point with respect to Fermi level which leads to localized p- and n-type doping effects in the graphene substrate.

STM, STS and Low-Energy Electron Diffraction (LEED) measurements were carried out on iridium (Ir) modified Si(111) and Si(100) surfaces. The Ir-modified Si(111) surface exhibited a $\sqrt{7} \times \sqrt{7}R19.1°$ domain formation that was composed of Ir-ring clusters. LEED measurements showed that on Ir-modified Si(100), a $p(2 \times 2)$ structure arose after annealing at $\sim 700℃$. The proposed model for the Ir-silicide nanowires shows that an Ir atom replaces every other Si dimer along the Si dimer rows of Si(100)-2×1.

CHAPTER I

INTRODUCTION

"There's Plenty of Room at the Bottom" is the title of the lecture given by Richard Feynman at Caltech back in 1959. In this lecture, he spoke about how it should be possible to write the entire Encyclopedia Britannica on the head of a pin, he also alluded to the possibility of using atomic manipulation for downscaling computer components or creating such devices like an electric motor at the molecular scale.[1] Since then, there have been multiple techniques such as Atomic Force Microscopy and Scanning Tunneling Microscopy, to name a couple, that have been developed to study and manipulate surfaces at the atomic scale. With the advent of these new techniques, Richard Feynman's predictions have been realized over the last 30 years.

In order to create atomic- or molecular-scale devices, two approaches can be employed. One is the "top-down" approach and the other is a "bottom-up" approach. In the top-down method, photo-lithographic techniques are used in conjunction with masks to etch substrates and then materials are subsequently deposited. However, the limits of photo-lithography are currently being reached since the cost to create smaller and faster components is extremely high and specialized equipment is needed to employ shorter wavelength sources such as extreme ultra-violet, x-rays or electrons for etching.[2] The "bottom-up" method involves growing or constructing components by the atom or molecule with atomic precision. This method is extremely time consuming and thus not feasible for mass production yet, there exists

a tactic to overcome this hurdle. Self-assembly of ordered structures can be obtained by utilizing physical interactions between atoms and/or molecules. Physical interactions include non-directional Van der Waals forces and directional hydrogen bonds. One can also make use of the natural morphology of surfaces to influence the formation of specific nano-structures such as wires, quantum dots, etc.[3-5]

In my dissertation, I focused on the self-assembly as a possible solution to scale-down components of integrated circuits. Below, you will find a brief introduction to each system that I have studied.

1.1: Porphyrins and Phthalocyanines on HOPG

On the chemically inert surface of highly ordered pyrolytic graphite (HOPG), the adsorption of molecules occurs via Van der Waals interactions which can hinder the control over the morphology of a monolayer. Even with the directional hindrance between molecule and substrate, large and uniform lamellae of molecules are still possible due to intermolecular forces such as hydrogen bonding and Van der Waals.[6-8] Using organic acids with long carbon chains on HOPG, Feng Tao, *et al.* showed that it is possible to grow self-assembled domains of well-ordered lamellae that span tens of nanometers. Various other molecules have been studied and found to create novel structures on the surfaces of silicon, copper, and platinum is in ultra-high vacuum (UHV) and at solid-liquid interfaces.[9,10]

Porphyrins have a delocalized conjugated π-electron system in a two-dimensional (2D) conformation that obey Huckel's rule.[11] Studies of self-assembling molecular nanostructures of porphyrins, specifically metallo-porphyrins, have been of great interest not only due to their

wide range of structural properties but also for their various optical properties that make them viable candidates for sensors, solar cells, catalysts for oxygen, and other molecular scale electronics.[12-18] Even if a porphyrin molecule has the same overall structure, the metal atom in the center can completely change the properties of the molecule. For example, depending on the metal atom, the porphyrin molecule will absorb only certain wavelengths of light. A previous study has shown that π-π interactions between porphyrin molecules can dictate how porphyrins adsorb on HOPG (flat or angled) or how they can interact with one another to form porphyrin stacks.[19] In Chapter 3, we address the following question: Is it possible to control the morphology of porphyrin thin films by just using physical interactions? A question remains of how these molecules might affect the substrate on which they are adsorbed and one of the most interesting surfaces that has unique attributes to investigate is graphene.

1.2: Graphene

Due to the chemical properties of carbon, carbon based molecules show a wide variety in their physical and chemical properties. So far, various allotropes of carbon have attracted attention such as carbon nanotubes, “bucky-balls”, and most of all graphene. Graphene is a true two-dimensional sheet of carbon atoms arranged on a honeycomb structure composed of hexagons.[20] Epitaxial growth of graphene on a silicon carbide surface is a promising method for the future of graphene-based electronics. Graphene has attracted a lot of attention for its unique properties that include the quantum Hall effect, massless Dirac fermions, long distance spin correlation, and gate control of electron or hole transport.[21-23] In 2008, hundreds of transistors were produced on a single graphene sheet by researchers at MIT Lincoln Lab.[24] In

2009, very high frequency transistors were produced at the Hughes Research Laboratories on monolayer of graphene epitaxially grown on silicon carbide (SiC).[25]

However, graphene has one major hurdle to overcome. Graphene is a gapless semi-metal and therefore it is not suitable for use in electronics that function off of a band gap. To induce a band gap in graphene, there have been studies on vacancies and substitutional impurities to modify the electronic properties, yet there are drawbacks to this method.[26] The drawback is that they significantly alter the mobility of charge carriers and the defect or impurity will act as a scattering source, effectively destroying the unique physical properties of graphene.[27,28] In order to avoid this problem, physisorption of molecules on the surface can induce charge transfer between the molecule and graphene. This functionalizes graphene by opening up a gap in the band structure as well as creating electron-rich or electron-poor regions in the graphene layer. Sun *et al.* performed first-principle calculations and photoemission spectroscopy to investigate the impact of strong acceptor and donor molecules adsorbed on a graphene surface and showed that graphene could be effectively p-doped or n-doped near the adsorbed molecules.[29]

Considering the importance of graphene as well as molecules like porphyrins and phthalocyanines, we wanted to bring them together and investigate effects of physisorption on graphene. In this dissertation, the effects of physisorbing of Zn-Phthalocyanine (Zn-Pc) onto graphene epitaxially grown on SiC were investigated with scanning tunneling microscopy (STM) and scanning tunneling spectroscopy (STS).

1.3: Iridium-Silicon Surfaces

Ir-silicides have the lowest (highest) Schottky barrier for holes (electrons). This makes them ideal for metal oxide semiconductor devices (e.g. MOSFET's) and infrared detection technology.[30,31] They are even more attractive than Pt-silicide which is commonly employed in large focal plane arrays for the detection of infrared wavelengths $(3-5\mu m)$.[32] The reason why Ir-silicides are more attractive than Pt-silicide for use in infrared detectors is due to the inherent cut-off wavelengths for photoemission. The Schottky barrier height between Pt and p-doped Si(001) is about $0.23eV$.[33] This corresponds to a cut-off wavelength of $5.4\mu m$. However, this cut-off wavelength needs to be extended in order to increase the sensitivity for longer wavelengths. Ir-silicide and p-doped silicon exhibits the lowest Schottky barrier of about $0.17eV$ and has a cut-off wavelength of $7\mu m$.[34] Due to these technological applications, there were extensive studies that focused on bulk properties of Ir-silicides epitaxially grown on Si(001) and Si(111).[35-39]

We are particularly interested in physical and electronic properties of metal-semiconductor systems due to their technological importance and the novel physical properties they exhibit. For example, it has been shown that alloying flat and/or vicinal silicon (Si) and germanium (Ge) substrates with various metals produces one-dimensional structures on the surface.[40-44] These one-dimensional structures, usually called nanowires, can be made up of any elements ranging to bismuth, transition metals and other rare-earth metals.[45-50] Among the possible nanowire systems, the nanowires made from gold and platinum hold a unique place. Their main advantage is that these 5d metals are resistant to oxidation which makes them

better candidates for device applications in ambient conditions. As you will see in the coming chapters, we successfully made Ir-Si nanowires on Si(001) and we also explored the morphology of Ir modified Si(111) surface. This surface is particularly interesting since instead of nanowires, the surface consists of Ir ring clusters similar to previously observed cobalt and nickel ring clusters on Si(111). Although there is extensive literature for almost all metal/silicon systems with various motivations, techniques and conclusions, it seems that the early stages of Ir growth on Si(111) and Si(001) surfaces have not been studied in detail.

CHAPTER II

MEASUREMENT METHODS

The experiments in this dissertation have been carried out on two different scanning tunneling microscopes (STMs). Solid-Liquid interface experiments were done with a Nanosurf EasyScan 2: STM under ambient conditions. Experiments carried out under Ultra-High Vacuum (UHV) conditions were performed with an Omicron variable temperature STM. Auger Electron Spectroscopy (AES) and low-energy electron diffraction (LEED) measurements were also performed under UHV conditions. This chapter is an overview of the physical principles behind the STM, LEED and AES systems and technical information for the experimental set-up.

2.1: UHV System and Components

The ultra-high vacuum system is custom built with one rough pump, one turbo pump and two ion pumps (with one ion pump containing a titanium sublimation system). To reach the standard operating pressure of $\sim 2 \times 10^{-10} mbar$, the system is initially baked at 140°C for 24 hours and allowed to pump down with the ion pumps for another 24 hour period. The UHV system houses three main measurement apparatuses, the STM, LEED and a Cylindrical Mirror Analyzer (CMA) for AES. A detailed picture is shown in Figure 2.1a and the LEED/Auger setup is shown in Figure 2.1b.

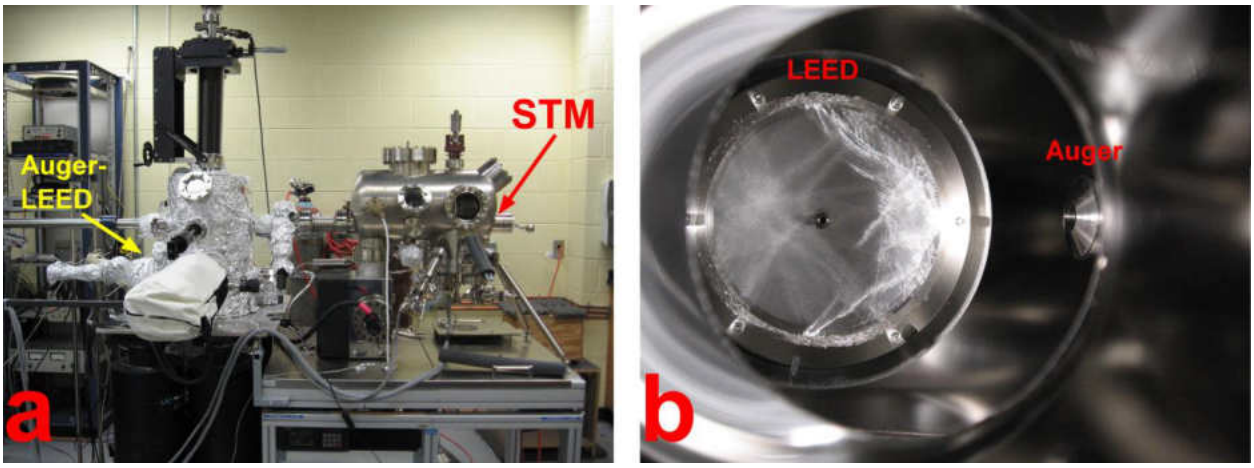

Figure 2. 1 (a) UHV system setup with a sample preparation chamber on left side and STM exclusively on the right side. (b) LEED screen and Auger CMA setup, 90° with respect to one another.

2.2: STM Theory

The basis of STM relies upon the quantum mechanical wave nature of electrons and their probability of tunneling across potential barriers. The potential barrier under UHV conditions is the vacuum gap in between the STM tip and the sample. However, for solid-liquid interface studies, the barrier is the solvent. A schematic of tip and sample electron tunneling in one-dimension is shown in Figure 2.2. When a voltage is applied to the tip/sample gap then contributions from both the work function difference and the applied voltage allow a range of energy for tunneling to occur (gray region in Figure 2.2c). Above the energy range, there are no electrons to contribute to tunneling and below the energy range there are no empty states for tunneling electrons to tunnel into.

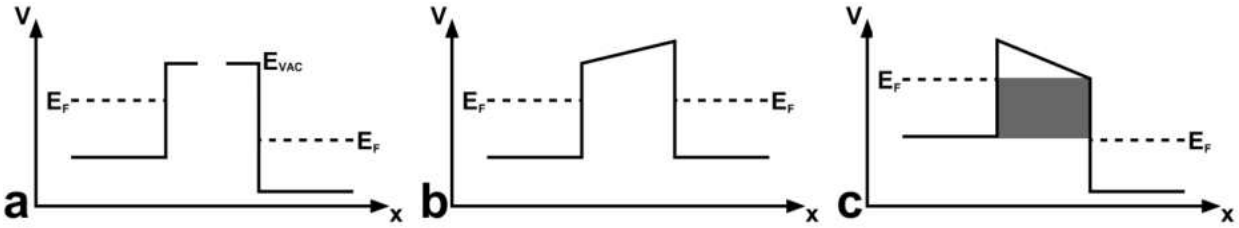

Figure 2. 2 One-dimensional representation of potential barriers. (a) Non-interacting system with energy E_{VAC}. (b) Tip and sample in equilibrium with common Fermi energies and the difference between work functions is depicted as an electric field in the gap. (c) An applied voltage promotes tunneling between tip and sample where the energies in the gray area can contribute to tunneling.

In order to calculate the tunneling between tip and sample, one needs to accurately determine the transmission coefficients across the potential barrier by knowing the work functions for the tip and the sample. However, this can become intractable as models cannot deal with complicated tip and sample structures. One way is to consider the tunneling current in first-order perturbation theory because the coupling between tip and sample can be treated as a weak interaction. In first-order perturbation theory the tunneling currents can be written as:

$$I = \frac{2\pi e}{\hbar}\sum_{s,t}\left[f(E_t)\left(1 - f(E_s + eV)\right)\right]\left|M_{s,t}\right|^2\delta(E_t - E_s) \qquad (1)$$

Where in Eqn. 1, $f(E)$is the Fermi function, eV is the applied gap voltage, $M_{s,t}$ is the tunneling matrix elements between states ψ_s (surface) and ψ_t (tip) with their respective energies E_s and E_t. Since most samples and tips used for STM are at room temperature or lower, the tunneling current equation can be further simplified by considering low temperature and low voltage limits. At low temperatures, the Fermi functions can be regarded as step functions near the Fermi energy since nearly all the states that contribute to tunneling are near the Fermi level. Next, for low voltage, the term in Eqn. 1 in square brackets can be further

simplified to a delta function and energies near E_F only need to be considered for both the tip and surface which gives the simplified form in Eqn. 2.

$$I = \frac{2\pi e^2}{\hbar} V \sum_{s,t} \left|M_{s,t}\right|^2 \delta(E_t - E_F)\, \delta(E_s - E_F) \tag{2}$$

Bardeen and Chen used approximations such as an s-orbital wave-function for the tip to show that at low voltages the tunneling matrix $M_{s,t}$ can have a continuum limit that relates the measured current to basically the density of states of the tip and the surface.[51,52] For the continuum limit consideration, another approach to calculate the tunneling current is to assign a density of states to both the tip and the sample, keeping in mind that the density of states of the surface depends on the position and their associated energies. Summing continuously over all contributing energies to tunneling, where ρ denotes the density of states, κ denotes the tunneling factor with the work functions ϕ of the surface and tip yields Eqn. 3.

$$I(V,r,z) = \int_0^{eV} \rho_s(r,E)\rho_t(E-eV)T(E,eV,r,z)dE \tag{3}$$

$$T(E,eV,r,z) = e^{-2z\kappa(E,eV,r)} \; and \; \kappa(E,eV,r) = \sqrt{\frac{2m}{\hbar^2}\left(\frac{\phi_s(r)+\phi_t}{2} + \frac{eV}{2} - E\right)}$$

$$\frac{dI}{dV} = e\rho_s(eV,r)T(eV,eV,r,z) + e\int_0^{eV} \rho_s(E,r)\frac{T(E,eV,r,z)}{d(eV)}dE \tag{4}$$

As shown above, the first term in the derivative of the tunneling current is proportional to the surface density of states. However, the tunneling rate term and its derivative (T and $dT/d(eV)$) are exponential functions and they can limit the resolution of the spectrum. In order to overcome this problem, Feenstra *et al*. suggested normalizing the derivative by

dividing it by the total conductance (Eqn. 5 and 6).[53] This is now a standard method of analyzing electronic properties of the surface and it is called the Local Density of States (LDOS). The LDOS curves can be derived from current vs. voltage curves (I-V curves), calculating the derivative numerically and normalizing or using a lock-in amplifier to physically measure the dI/dV vs. voltage curve.

$$LDOS \equiv \frac{{}^{dI}/_{dV}}{\left|{}^{I}/_{V}\right|} = \frac{dI}{dV}\left|\frac{V}{I}\right| \tag{5}$$

Normalizing Eqn. 4 yields the LDOS,

$$LDOS \propto \frac{e\rho_s(eV,r) + e\int_0^{eV} \frac{\rho_s(E,r)}{T(eV,eV,r,z)} \frac{dT(E,eV,r,z)}{d(eV)} dE}{\frac{1}{eV}\int_0^{eV} \rho_s(E,r) \frac{T(E,eV,r,z)}{T(eV,eV,r,z)} dE} \tag{6}$$

The lock-in amplifier can be used to physically measure derivatives of the tunneling signal. To do this, a sine-wave with a reference frequency (in our case, supplied by the trigger of a function generator) is added to the input voltage V_{DC} of the STM control unit. The added AC signal has a small voltage V_ω with respect to the applied DC voltage from the STM and therefore the modulated tunneling current can be expanded as a Taylor series, see Eqn 7.

$$I(V_{DC} + V_\omega \cos \omega t) = I(V_{DC}) + \left(\frac{dI}{dV}\right)_{V_\omega} V_\omega \cos \omega t + \frac{1}{2}\left(\frac{d^2I}{dV^2}\right)_{V_\omega} V_\omega^2 \cos^2 \omega t + \cdots \tag{7}$$

Using the trigonometric double-angle formula, Eqn. 7 can be expanded further:

$$I(V_{DC} + V_\omega \cos \omega t) = I(V_{DC}) + \left(\frac{dI}{dV}\right)_{V_\omega} V_\omega \cos \omega t + \frac{1}{4}\left(\frac{d^2 I}{dV^2}\right)_{V_\omega} V_\omega^2 +$$

$$\frac{1}{4}\left(\frac{d^2 I}{dV^2}\right)_{V_\omega} V_\omega^2 \cos 2\omega t + \cdots \quad (8)$$

Then, the modulated response signal is received from the STM measurement. In order to get the first derivative, the signal is multiplied by a sine-wave at the reference frequency ω with a phase separation so that only the first harmonic of the response signal is non-zero. Thus, the amplitude of the first harmonic is proportional to the first derivative of the tunneling current. By multiplying at higher multiples $(2\omega, 3\omega, etc.)$ of the reference frequency, one may get higher order derivatives but those are for other physical values (not discussed here).

It is all well and good that one can get the spectroscopy of a surface but incorporating the STS function *while* taking and STM image, now that's truly useful and necessary to gain insight to surface states. A simultaneous STM and STS measurement allows one to determine spatial differences in the spectroscopies so not only will the energies be known but also the spatial location of states on a surface. This can be extremely useful to see the effects of deposited atoms or molecules onto substrates and their localized effects on the states.

2.3: Low Energy Electron Diffraction

Low energy electron diffraction (LEED) makes use of elastically scattered electrons and the wave nature of electrons to produce a diffraction pattern which allows one to probe the lattice structure(s) of a surface. The surface sensitivity arises from the low energy of the incident electrons and their large cross section for inelastic scattering which only allows the

incident electron to penetrate to a depth of about 1nm (about 3-4 atomic layers). The source for inelastically scattered electrons is primarily from interactions with collective excitations such as plasmons and phonons.

In LEED, low energy electrons are accelerated towards a surface by an electron gun and the elastically backscattered electrons are observed with a phosphorescent screen. A schematic of the LEED instrument is shown in Figure 2.3a. A tungsten filament is heated by direct current generating free electrons at the kink of the filament. A voltage is applied to the compartment (electron gun) which houses the tungsten filament (not shown) which creates an essentially mono-energetic, collimated electron beam that strikes the sample. In order to collect the elastically backscattered electrons, a series of grids are employed to remove the inelastically scattered electrons from reaching the phosphorescent screen. The positions of the LEED spots on the phosphor screen are a function of both electron energy and the surface crystal structure.

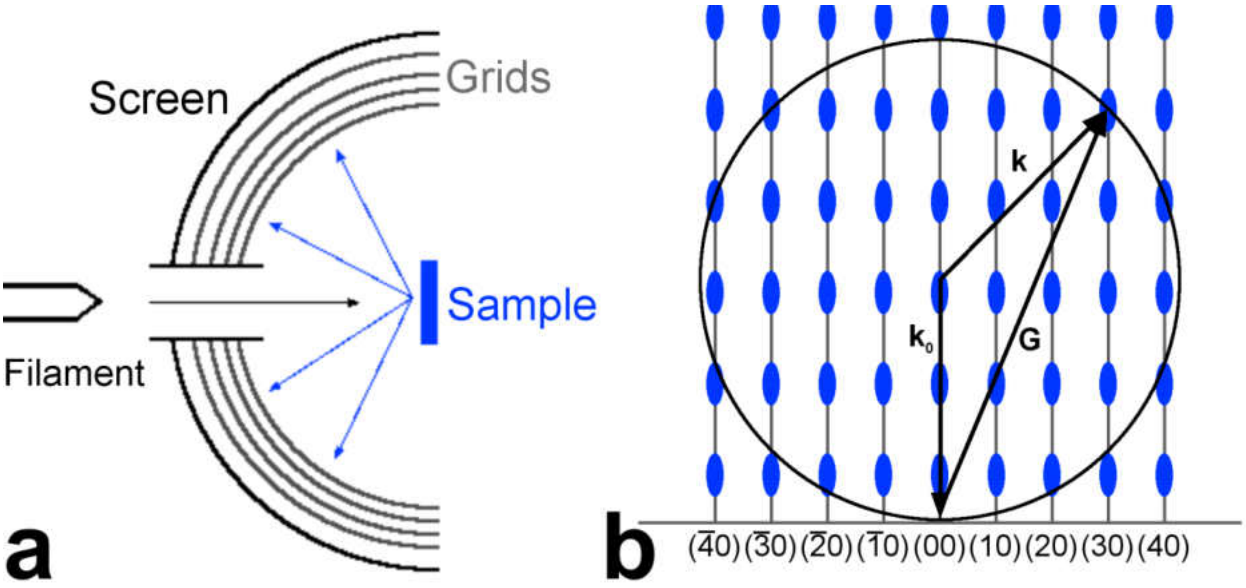

Figure 2. 3 (a) Schematic of LEED setup with sample. (b) Ewald construction of surface scattering where diffraction pattern is the rods vertical to the surface.

To obtain a diffraction pattern, the Laue condition (Eqn. 9) must be satisfied for wave vectors parallel to the surface, where the reciprocal lattice vector $\vec{G}_{||}$ must be equal to the difference of the incoming wave vector $\vec{k}_{0||}$ and the diffracted wave vector $\vec{k}_{||}$. The Ewald construction for surface scattering is depicted in Figure 2b, where the vertical lines denote the diffracted pattern that can be observed on the phosphorescent screen. The ovals denote larger intensities of the diffraction pattern if the Laue condition for the perpendicular component of the scattering vector is approximately met.

$$\vec{G}_{||} = \vec{k}_{0||} - \vec{k}_{||} \tag{9}$$

2.4: Auger Electron Spectroscopy

Auger electron spectroscopy (AES) is one of the most reliable means to study chemical data of surfaces. AES relies on the Auger-process which can be described in three steps. First,

an incoming electron creates an excitation in an atom which can ionize the atom by causing emission of one of the core level electrons, leaving a hole. Since this excited state is energetically unfavorable, one of the outer shell electrons will then decay to the empty core state by emitting energy. This emitted energy will in turn be absorbed by another outer shell electron which will subsequently be emitted from the atom with a specific kinetic energy that is characteristic of the transitions that took place in that atom. The most common transitions are KLL and LMM but there are others as well such as those that include the valence electrons denoted LMV, LVV, etc. The characteristic kinetic energy of the Auger-electron can be approximated by Eqn. 10 where E_{core} is the core electron's energy, E_1 is the energy level of the outer shell electron that decayed, and E_2 is the energy level of the emitted Auger-electron.

$$E_{Kin} = E_{core} - (E_1 + E_2) \tag{10}$$

The emitted Auger-electrons are then analyzed with a double pass cylindrical mirror analyzer (CMA) which is depicted in Figure 4. In the case of the CMA2000, the inner cylinder is held at ground potential while the applied voltage on the outer cylinder is scanned for various pass energies. The electrons that pass enter an electron multiplier to amplify the signal. Signal detection is also facilitated by modulating the outer cylinder voltage at 2.5 kHz and detecting the 5 kHz component by means of a lock-in amplifier. The resulting spectrum is the first-derivative (dN/dE) of the electron energy distribution curve $N(E)$. In this first-derivative, the intensity ratio of each peak correlates to the ratio of elements on the surface and along with STM measurements an accurate surface coverage can be calculated.

The signal intensity of a substrate (S) covered by a fraction ϕ_A of a monolayer of an adsorbate (A) can be written as:

$$I_S = I_S^* \left(1 - \phi_A + \phi_A e^{\frac{-a_A}{\lambda_A(E_S)\cos\theta}}\right) \tag{11}$$

And the signal from the over layer can be respectively written as:

$$I_A = I_A^* \phi_A \left[\frac{1 + r_S(E_A)}{1 + r_A(E_A)}\right] \left(1 - \phi_A e^{\frac{-a_A}{\lambda_A(E_A)\cos\theta}}\right) \tag{12}$$

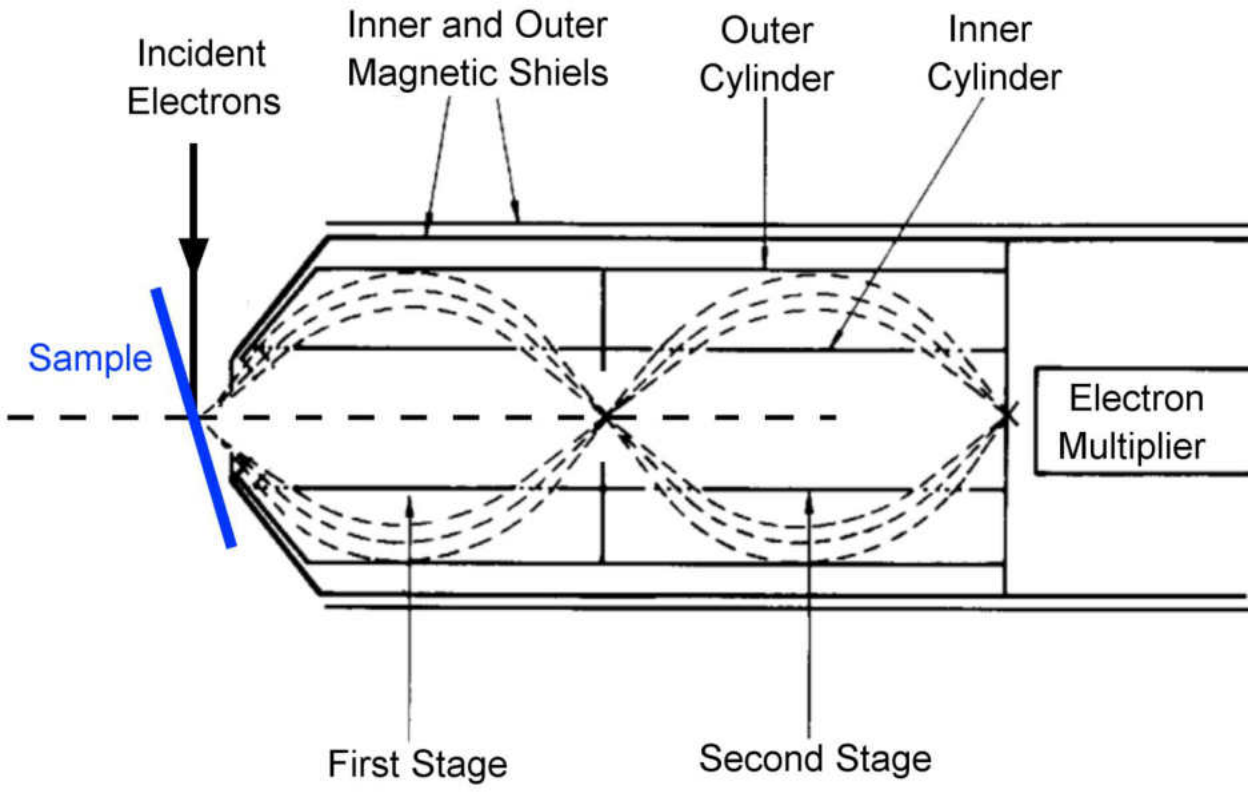

Figure 2. 4 Schematic of AES setup with sample set at a grazing angle with respect to incident electrons.

Where, I_A and I_S are the intensities of the signal from the adsorbate and substrate, respectively -and I_A^* and I_S^* are the intensities that would be measured from pure substances of the adsorbate and substrate. Also in Eqn. 12, r_S and r_A are back-scattering terms, λ_A is the elastic mean free path of electrons at the respective energies E_S and E_A, θ is the angle of emission with respect to the surface normal, and a_A denotes the atomic size of the adsorbate. However, it does not make much sense to measure these intensities since the comparison between the pure and mixed states for the intensities cannot be measured at the same time and other factors like sample roughness come into play, therefore only ratios can truly be considered. Thus, from Eqn. 9 and Eqn. 10, the fractional monolayer coverage ratio is given by:

$$\frac{\phi_A\left(1-e^{\frac{-a_A}{\lambda_A(E_A)\cos\theta}}\right)}{1-\phi_A\left(1-e^{\frac{-a_A}{\lambda_A(E_S)\cos\theta}}\right)}=\left[\frac{1+r_A(E_A)}{1+r_S(E_A)}\right]\frac{I_A/I_A^*}{I_S/I_S^*} \tag{13}$$

Eqn. 13 is the equation that is used to calculate surface coverage ratios and was employed to calculate the coverage of iridium on silicon surfaces in Chapter 5 and 6 of this dissertation.

CHAPTER III

PHYSISORPTION OF MOLECULES ON HOPG

Porphyrins and phthalocyanines have a nearly square core conformation and they have a delocalized π-electron system. Metal porphyrins are the focus of extensive studies as they have unique properties that make them valuable for device applications in areas such as light-emitting diodes, organic displays, and thin film transistors.[54,55] In addition to this, metal porphyrins constitute the active centers of biologically important molecules such as heme and chlorophyll.[56,57] There are extensive studies of thin films of these molecules in ultra-high vacuum and at solid-liquid interfaces.[58-60] The feasibility of these technological applications partly depends on the quality and properties of the thin films of these molecules. In order to contrive building novel molecular structures of porphyrins, one can employ physical interactions between adsorbed molecules as wells as between the molecules and substrate. These physical interactions include non-directional van der Waals forces and directional hydrogen bonds. On a chemically inert surface such as highly-ordered pyrolytic graphite (HOPG), the adsorption of molecules occurs via van der Waals interactions which hiders the control over the morphology of the thin film. Even though the molecule-substrate interaction is non-directional, it is still possible to compile large and uniform lamellae of molecules with the help of directional intermolecular forces, such as hydrogen bonding.[61,62]

Formation of porphyrin chains has been reported before.[63-65] However, these porphyrin chains form with the aid of long carbon tails that are attached to the porphyrin core itself via chemical bonds. In this chapter, we want to illustrate an alternative technique that employs only physical interactions between porphyrin molecules and long chain acids to control and build novel porphyrin structures and to explicitly show how different central-atom complexes in the same porphyrin core can influence the formation of novel structures such as a uniform lamellae and molecular chains.

3.1: 5-OIA Assisted Growth of Metal-TCPP Domains on HOPG

We chose two similar molecules, Copper(II) *meso*-tetra (4-carboxyphenyl) porphyrin (Cu-TCPP) and Iron(III) *meso*-tetra (4-carboxyphenyl) porphyrin Chloride (Fe-TCPP), diagrams shown in Figure 3.1.[66,67] As their names suggest, the only difference between these two molecules is the central metal complex where Cu-TCPP has only a Cu atom and Fe-TCPP has an iron-chloride complex (See Figure 3.1). The central metal atom significantly changes the morphology of thin films of porphyrin molecules which has been shown before in a sequence of studies on platinum, nickel and vanadium-oxide octaethyl-porphyrin molecules adsorbed on bare and 5-OIA modified HOPG surfaces. [68,69]

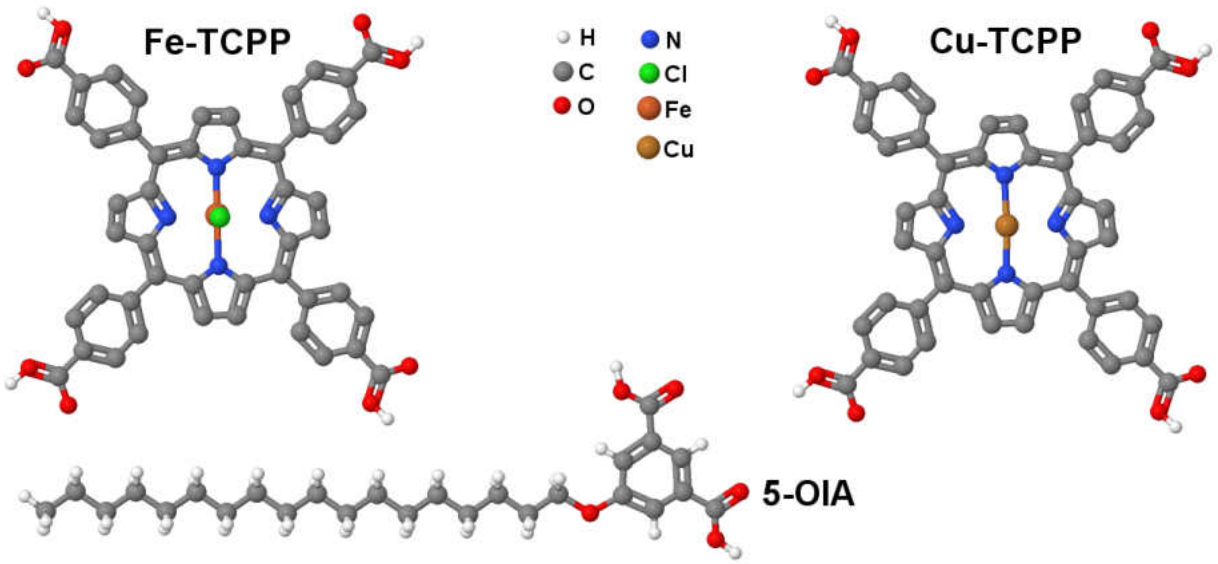

Figure 3. 1 Schematics of Fe-TCPP, Cu-TCPP, and 5-OIA molecules.

Another reason to choose these specific molecules was to employ intermolecular hydrogen bonding from their carboxyl (COOH) groups. The carboxyl groups are attached to the porphyrin core through phenyl rings (See Figure 3.1). The existing carboxyl groups in the TCPP molecules makes them ideal molecules to study 2-D networks of hydrogen bonded porphyrins. Studies on various derivatives of the TCPP molecules showed that the phenyl rings of TCPP do not lay parallel to the surface. This geometry of phenyl groups weakens the van der Waals interactions between the molecules and the HOPG surface. This makes them highly mobile on the surface and prevents them from forming stable thin films.[70] One method to solve this problem is to use a binary solution. A binary solution has both the target molecules and a secondary molecule which readily forms a stable layer on the surface.[71,72] Typically, the secondary molecules are long chain acids which form 2-D domains with the help of van der Waals interactions and hydrogen bonding. 2-D domains of these acids are ideal to cover up the

otherwise featureless morphology of HOPG surface and pin down the target molecules. In this project we chose, 5-(Octadecyloxy) Isophthalic Acid (5-OIA) as a secondary molecule.

3.2: Experimental

Cu-TCPP and Fe-TCPP were both purchased from Frontier Scientific. 1-Phenyloctane (98%) and 5-OIA (98%) were purchased from Aldrich. 1-Phenyloctane was used as a solvent. Both Cu-TCPP, Fe-TCPP and 5-OIA were used without further purification. STM tips were mechanically cut from Pt-Ir (0.8-0.2 alloy) $0.25\,mm$ diam. wire purchased from Nanoscience Instruments. HOPG substrates were purchased from Nanoscience Instruments and mechanically cleaved using scotch tape. Experiments were performed at the solid-liquid interface and under ambient conditions using a NanoSurf® EasyScan2 STM. Cu-TCPP and Fe-TCPP molecules don't dissolve very well in 1-phenyloctane $(< 10^{-4} Mol)$ however the secondary 5-OIA molecule dissolves very well. In this study, only saturated solutions of TCPP and 5-OIA molecules were used.

3.3: Results & Discussion

5-OIA is a special di-acid in the sense that two carboxylic acid groups bonded at the 3- and 5-position of its phenyl ring head group. Since there are two opportunities for hydrogen bonding at one end of the molecular chain, 5-OIA molecules form interesting supramolecular structures on HOPG. A saturated solution of 5-OIA molecules covers majority of the surface almost instantly. Two adjacent 5-OIA molecules in a domain assemble with opposite faces in order to maximize the van der Waals interactions and Lei *et al.* showed that the head groups form three O–H–O bonds and forms rows that are visible in Figure 3.2a.

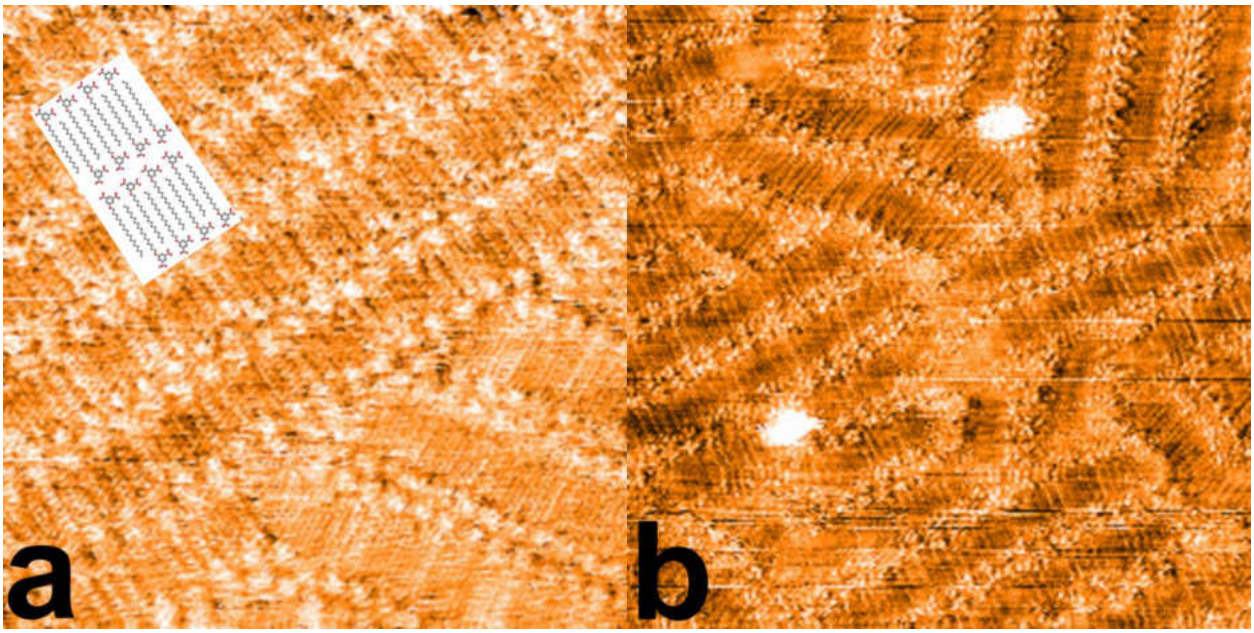

Figure 3. 2 (a) $19.1\,nm \times 19.1\,nm$ STM image of 5-OIA on HOPG, $V_{tip} = 0.88\,V, I = 0.45\,nA$. (b) $25.2\,nm \times 25.2\,nm$ STM image of two Cu-TCPP molecules (two white blobs) adsorbed on 5-OIA modified HOPG surface, $V_{tip} = 1.1\,V, I = 0.6\,nA$.

The typical surface coverage of Cu-TCPP molecules is less than 3%. However, this seemingly disadvantageous situation was used in favor of observing individual porphyrins, and porphyrin chains. Figure 3.2b shows an STM image of two individual (white blobs) Cu-TCPP molecules adsorbed on 5-OIA covered HOPG surface. 5-OIA molecules create diffusion barriers high enough to stabilize individual Cu-TCPP molecules. We believe that the interaction between 5-OIA and Cu-TCPP molecules is through the carboxyl groups of these molecules. Similar interlayer interactions between the hydrogen bonds of each layer were observed on various cases.[73-75] Although, single Cu-TCPP molecules were immobile enough to be imaged, they still have some degrees of freedom which prevented getting better resolution images of these molecules.

Cu-TCPP chains are the most common form of structures observed on the surface and an example of a porphyrin chain is in Figure 3.3a. The length of the chains can easily reach up to

hundreds of nanometers. The distance between individual Cu-TCPP molecules along the chain range from $1.4\,nm$ to $1.9\,nm$, showing that Cu-TCPP molecules can be separated further than the length of a typical hydrogen bond. In addition to this, usually, Cu-TCPP chains follow the boundaries between 5-OIA domains. However, in the absence of a domain boundary Cu-TCPP molecules follow the phenyl groups of 5-OIA molecules. These common trends for chains on the head-groups of 5-OIA suggests that the interaction between carboxyl groups of 5-OIA layer and Cu-TCPP molecule plays a significant role in the formation and the stabilization of Cu-TCPP. A computational study which takes into account on various adsorption sites and geometries is required to obtain a better model for the chain.

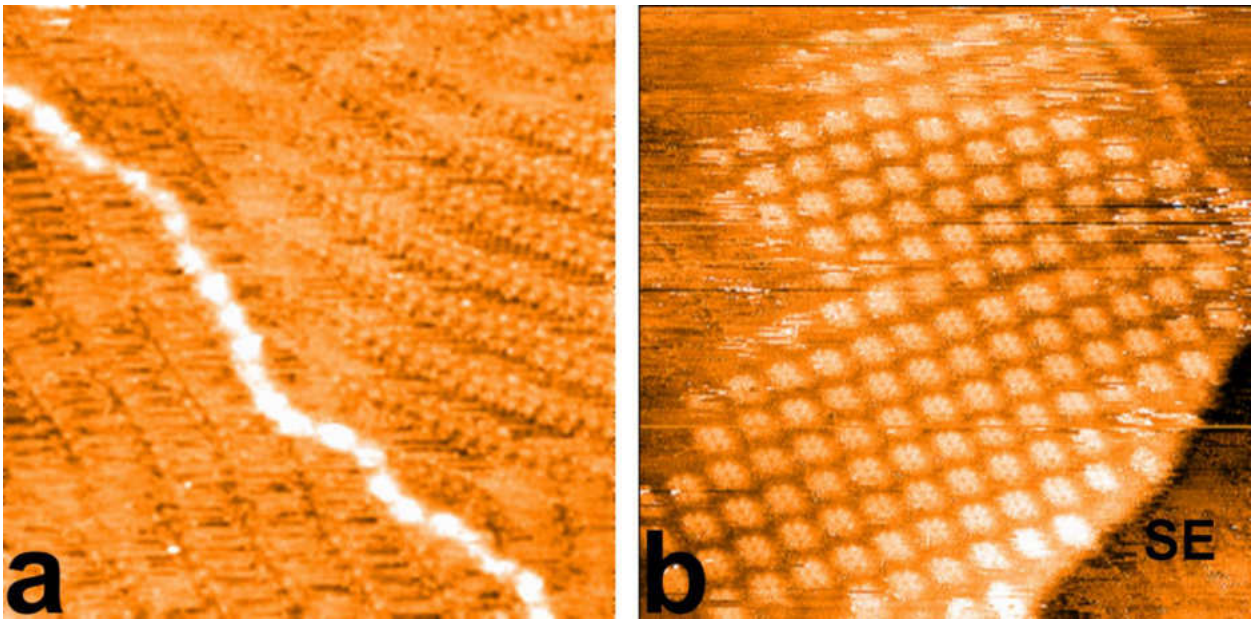

Figure 3. 3 (a) $29.4\,nm \times 29.4\,nm$ STM image of Cu-TCPP chain over 5-OIA head groups, $V_{tip} = 1.2\,V, I = 0.7\,nA$. (b) $30.5\,nm \times 30.5\,nm$ STM image of Cu-TCPP 2-D patch building next to a step edge (denoted by SE), $V_{tip} = 1.2\,V, I = 0.6\,nA$.

Cu-TCPP molecules adsorbed on 5-OIA layer can also form a rectangular lattice (see Figure 3.3b) with unit cell vectors of $(2.17 \pm 0.03\,nm)\hat{x}$ and $(1.95 \pm 0.04\,nm)\hat{y}$. However, a patch was only observed along a step edge (denoted SE in Figure 3.3b). A former study by Lei,

et al. on 5,10,15,20-tetrakis (4-carboxylphenyl)-21H,23H porphyrin (H-TCPP) adsorbed on bare HOPG surface with the help of stearic acid showed that the H-TCPP molecules form a square lattice and the unit cell vectors are about $1.9\,nm$. Absence of any relation between the absorbed Cu-TCPP molecules and the underlying 5-OIA layer indicates that the driving force to form these 2-D domains are the intralayer interactions between Cu-TCPP rather than inter-layer interactions between Cu-TCPP and 5-OIA molecules.

We have repeated the aforementioned experiments by using Fe-TCPP and 5-OIA solutions hoping that a different central metal complex would lead to a change in the interaction between the porphyrin and 5-OIA molecules and lead to the formation of porphyrin chains. Figure 3.4a shows that, once deposited onto HOPG surface, the solution leads to the formation of three different domains i.e. 5-OIA domain, Fe-TCPP/5-OIA chains and an oblique domain that co-exist on the surface. The size of the unit cell vectors measured on Fe-TCPP molecular chains are $(2.21 \pm 0.21\,nm)\hat{x} \times (3.30 \pm 0.14\,nm)\hat{y}$ and the angle between the lattice vectors is $\theta = 86.9 \pm 0.2°$. The measured $3.3\,nm$ spacing between the Fe-TCPP/5-OIA chains is about $0.4\,nm$ larger than the spacing between the rows of 5-OIA molecules alone. Based on the experimental data, we proposed the following tentative model in which the chloride ion at the center of a porphyrin molecule moves in between the head groups of 5-OIA molecules and pins the porphyrin molecules into this new type of superlattice, see Figure 3.4b. It is not possible to find out the orientation of the phenyl groups from the STM images. Therefore, in order to keep the model perceptible we ignore the rotational freedom of the phenyl groups and show them lying flat on the surface. However, if we consider the rotational freedom of phenyl groups, we can speculate about possible hydrogen bonds between Fe-TCPP

molecules and the underlying 5-OIA layer. Unlike smaller 5-OIA domains, the domains of Fe-TCPP/5-OIA chains can stretch up to tens of nanometers. This also provides additional proof that the chains of Fe-TCPP molecules are not simply formed by Fe-TCPP molecules adsorbed on the head groups of 5-OIA molecules but instead these two molecules with rather different geometries work together to form these molecular chains.

As we mentioned before, the chains of Fe-TCPP/5-OIA molecules are not the only domain that exists on the surface. Figure 3.4c shows high-resolution STM images of one of these oblique domains. The lattice vectors for the uniform oblique domain of Fe-TCPP molecules are $(4.0 \pm 0.10\ nm)\hat{x} \times (3.01 \pm 0.17\ nm)\hat{y}$ with $\theta = 113.3 \pm 1.5°$. In an oblique domain, the surface coverage becomes approximately 0.08 Fe-TCPP molecules per nm^2. The oblique rings that can be attributed to the carboxyphenyl groups of the Fe-TCPP molecules (blue dots) and the underlying 5-OIA carboxyphenyl groups (green dots). A combination of these six carboxyphenyl groups and their electronic contribution gives a rather unusual hexagonal appearance to the Fe-TCPP molecules.

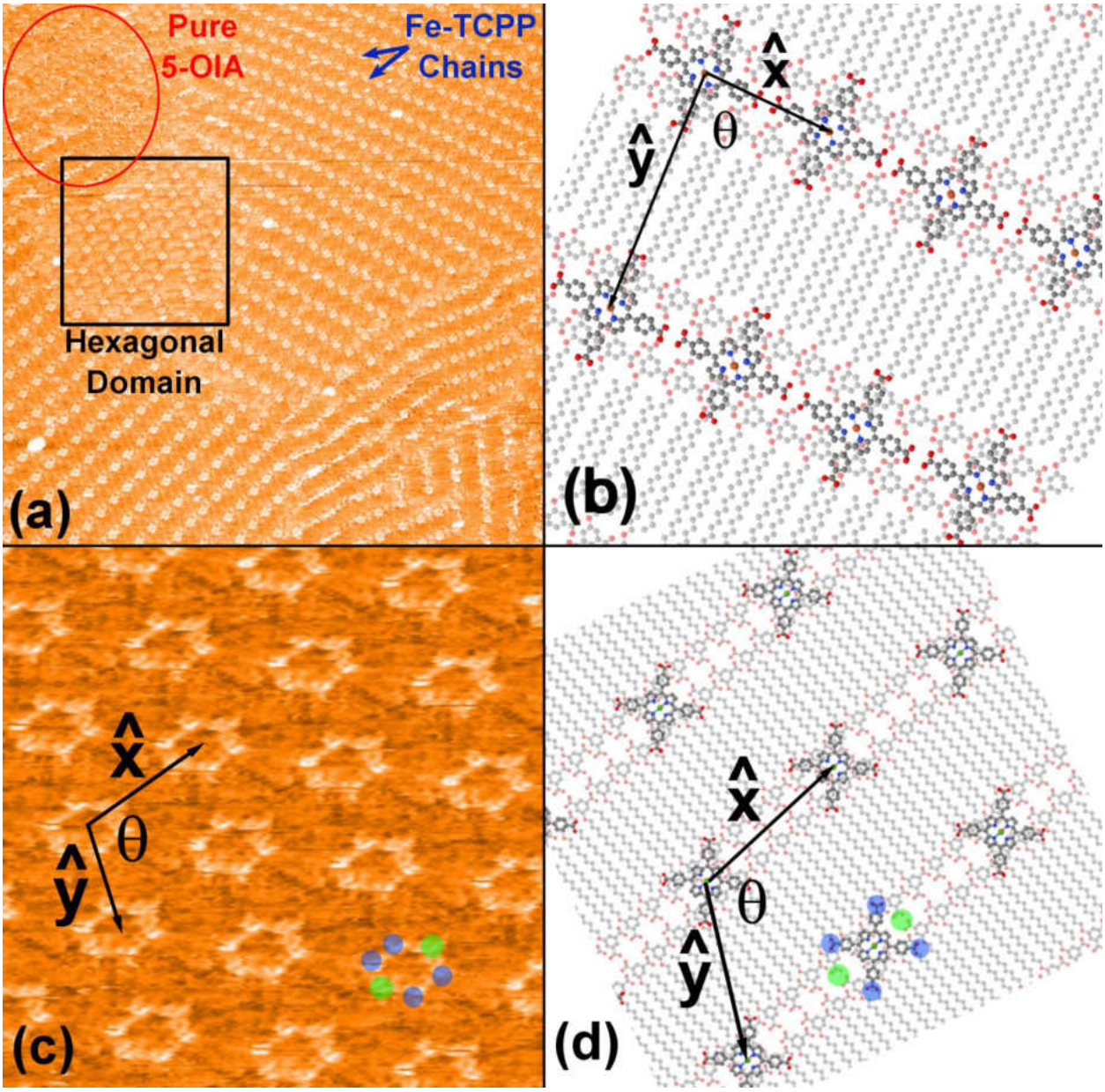

Figure 3. 4 (a) $100\ nm \times 100\ nm$ STM image of Fe-TCPP and 5-OIA domains, $V_{tip} = 1.1\ V, I = 0.4\ nA$. (b) Schematic of Fe-TCPP chains over the head groups of 5-OIA. (c) $30\ nm \times 30\ nm$ STM image of Fe-TCPP hexagonal domain, $V_{tip} = 1.1\ V, I = 0.18\ nA$. (d) Schematic of hexagonal domains, again with Fe-TCPP over the head groups of 5-OIA.

In order to provide experimental proof for the proposed models above, we came up with the following experiment. We deposited 5-OIA molecules on freshly cleaved HOPG surface from a saturated solution of 5-OIA dissolved in 1-phenyloctane. We confirmed the formation of 5-OIA layer with the STM. Then a small drop of Fe-TCPP solution (solvent is acetone) was placed

on the STM tip. Once the acetone was evaporated, the tip had miniscule amount of Fe-TCPP molecules. The STM images measured right after immersing the tip into the thin film of 5-OIA solution (solvent is 1-phenyloctane) on HOPG showed that the surface is uniformly covered by oblique domains. Since the surface was initially covered with 5-OIA layer, the observation of oblique domains of Fe-TCPP molecules prove that for this particular domain Fe-TCPP molecules simply lie down on top of 5-OIA molecules. We repeated this experiment with different tips and freshly prepared samples but we never observed the formation of Fe-TCPP/5-OIA chains indicating that the formation of these chains requires co-adsorption of Fe-TCPP and 5-OIA molecules. In order to reveal 5-OIA molecules underneath the Fe-TCPP molecules, we scanned the surface with low voltage-high current settings (specifically $0.1\ V$ and $1.0\ nA$). Under these conditions, the tip moves closer to the surface and pushes the porphyrin molecules away. Once we zoomed out and scanned the surface at usual tunneling settings, we observed that the oblique domain of Fe-TCPP is partly removed and the 5-OIA layer became visible once again.

The difference in the morphology of Cu-TCPP chains and Fe-TCPP/5-OIA chains clearly supports the basis of how important the central metal atom is to the morphology of porphyrin thin films. Studies involving other porphyrin derivatives on various substrates with no co-adsorbed molecules show that porphyrins can form close-packed hexagonal domains with lattice spacing of about $1.0\ nm$.[76,77] Such close-packed domains were also observed when porphyrins are co-adsorbed with 5-OIA molecules. This happens only when the molecule-molecule interaction is much stronger than molecule substrate interaction.

3.4: Conclusion

In summary, binary solutions of Cu-TCPP/5-OIA and Fe-TCPP/5-OIA were measured with an STM at solid-liquid interface under ambient conditions. We showed that 5-OIA molecules facilitate a means to anchor TCPP molecules on HOPG surface to form chains and other novel structures. The formation of porphyrin chains in both cases prefer to get adsorbed on the head groups of 5-OIA and in the case of Cu-TCPP, the chains prefer to grow along domain boundaries of the 5-OIA layer. We think that this is because of the fact that not all the carboxyl groups of TCPP molecules are used while forming the chain, therefore, the unused carboxyl groups, with the ability to make hydrogen bonding, interact with the 5-OIA molecules. The question arises on what effect molecular adsorption has on a substrate and this merits further investigation. Hence a study on monolayer graphene is a very promising surface to focus upon.

CHAPTER IV

PHYSISORPTION OF MOLECULES ON EPITAXIAL GRAPHENE

Graphene is a single-atomic-layer of carbon atoms in a sp^2 hexagonal bonding configuration making it one of the strongest materials in nature. This two-dimensional allotrope of carbon comes in a few forms such as a planar monolayer, carbon nanotubes which are essentially graphene sheets rolled upon itself and arguably C_{60} ("Bucky balls"). Compared to other nanomaterials, graphene is unique in the sense that the lateral dimensions of graphene are up to tens or hundreds of micrometers while the thickness is only one atom and still can be seen with a visible light microscope.[78] In addition to the strength of the sp^2 hybridized bonds, they also have delocalized π-orbitals parallel to the surface. The delocalized π-orbitals lead to the zero-gap, semi-metal nature of graphene and Dirac cones/points along the K- and K'-points of the Brillouin zone. The reason the term Dirac point is used is because a linear relationship can be derived from the Dirac equation:

$$E = \sqrt{(mc^2)^2 + (pc)^2} \tag{11}$$

If there is a particle that is massless, then the first term in Eqn. 11 drops out yielding the relationship in Eqn. 12 (Figure 4.1a). Electrons in graphene near the K-point follow the same linear dispersion relation, therefore any electrons at this energy and momentum are considered as massless Dirac fermions.

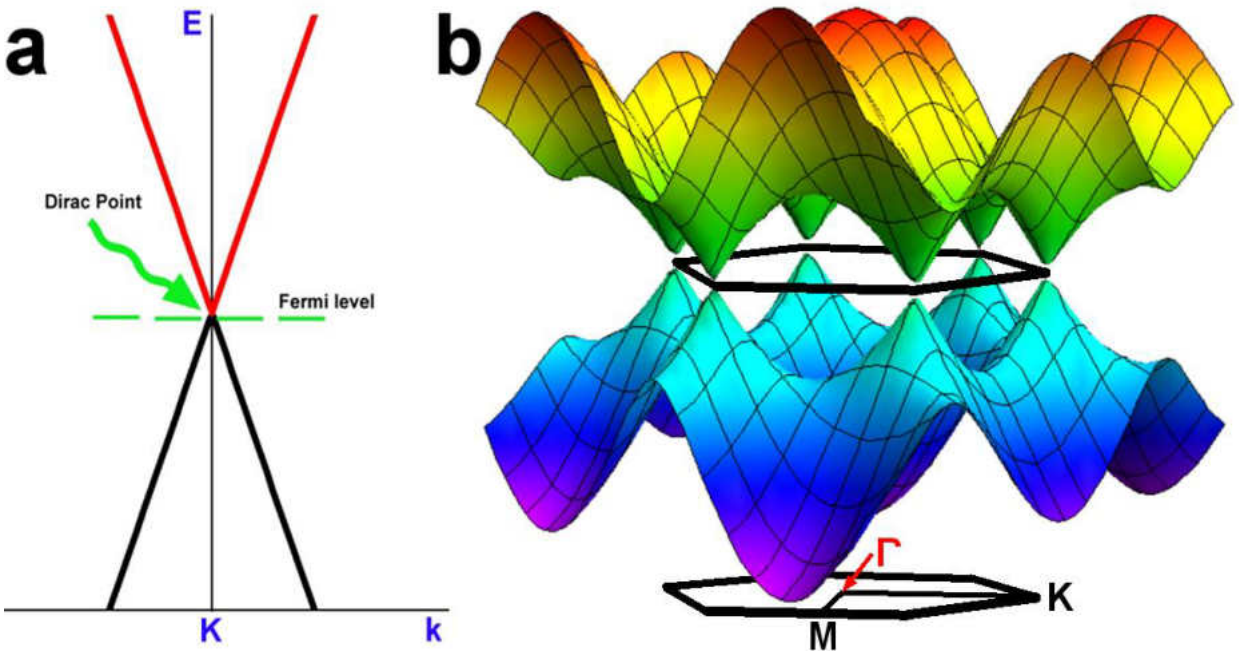

Figure 4. 1 (a) Two-dimensional band structure of graphene showing the Dirac point at the K-point and Fermi level.

$$E = pc \propto k \tag{12}$$

The band structure of graphene can be described fairly well by considering nearest- and next-nearest-neighbor interactions in the tight-binding model, such as that given by Wallace in 1947.[79] The other, more well-known tight-binding approximation was developed by Saito *et al.*, where they made an approximation of a non-finite overlap between the basis functions and only included nearest-neighbor interactions.[80] In their work, Saito *et al.* showed that the dispersion relation can be expressed as Eqn. 13 (depicted in 3-dimensions in Figure 4.1b). In Eqn. 13, $\gamma \approx 2.8\ eV$ and $a = 2.46\ \dot{A}$.

$$E = \pm\sqrt{\gamma^2\left(1 + 4\,Cos^2\left(\frac{k_y\,a}{2}\right) + 4Cos\left(\frac{k_y\,a}{2}\right)Cos\left(\frac{k_x\,a}{2}\right)\right)} \tag{13}$$

Overall, it is the massless behavior of electrons in graphene that leads to the properties of ballistic conduction along the K direction where electrons can travel over one hundred nanometers with a very low probability of scattering. The low probability of scattering also leads to a long-distance spin correlation which makes graphene extremely attractive for use in spintronics. For these very reasons, graphene based electronics are very promising. However, a band gap is needed in order to realize graphene based transistors. This is the basis for our work on physisorbing molecules onto a graphene surface and investigating the effects of their presence on the Dirac point.

For our experiments, it was imperative that we chose a molecule that would be able to adsorb on the chemically inert surface of graphene via van der Waals interactions as well as a molecule that has both donor and acceptor atoms within its structure. The donor/acceptor atoms would provide a very strong comparison of localized effects on the surface density of states. Hence, the molecule Zinc(II)-Phthalocyanine tetrasulfonic acid (Zn-Pc) was chosen. A schematic of the Zn-Pc molecule is shown in Figure 4.2. The Zn complex at the core will be able to serve as a donor site while the electronegative sulfonic acid groups on the perimeter will serve as acceptors.

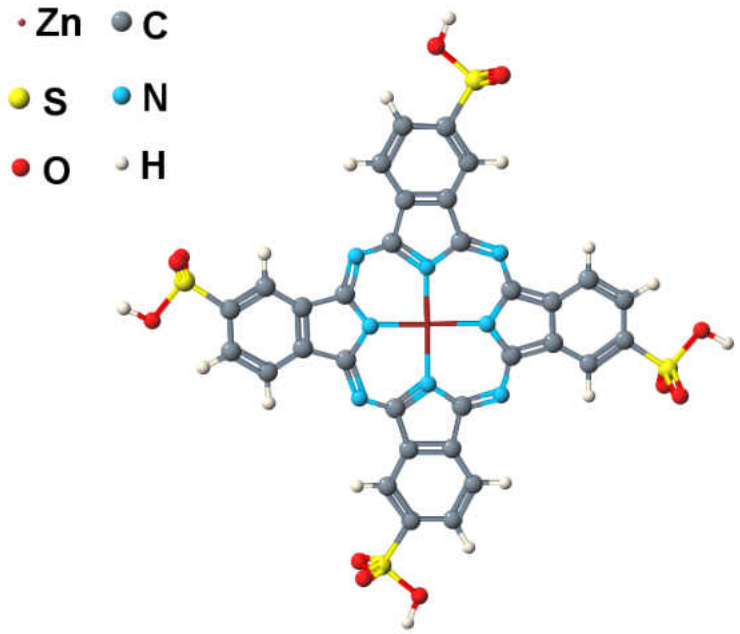

Figure 4. 2 Schematic of Zn-Pc molecule.

4.1: Experimental

The experiments were performed in UHV using an Omicron Variable Temperature STM and LEED to characterize the surface. Zinc(II)-Phthalocyanine tetrasulfonic acid (Zn-Pc) was purchased from Frontier Scientific and was used as purchased. The 6H-SiC(0001) samples were mechanically cut, washed with isopropanol, and loaded into UHV as purchased from University Wafer. The SiC samples were then degassed at $\sim 400°C$ for 24 hours and then flash annealed multiple times at $\sim 1300°C$ while keeping the pressure ($P \leq 1.0 \times 10^{-9} mbar$) by direct current heating. Once a clean monolayer graphene layer was confirmed with LEED and STM, Zn-Pc was deposited via two methods.

Due to the chemical passivity of graphene, the SiC surface that was covered with graphene could be exposed to atmosphere briefly with no noticeable contamination (results not shown). Once exposed to atmosphere, Zn-Pc dissolved in isopropanol was deposited onto

the surface (**method 1**). Zn-Pc was dissolved to create a saturated solution. Once the solution was deposited, the sample was immediately loaded back into high vacuum with enough time to allow the 1-phenyloctane to evaporate ($\sim$1hr) and then loaded into UHV for STM measurements. The second deposition method was via a home-built Knudsen cell that was used to thermally evaporate Zn-Pc onto the graphene surface. The Knudsen cell was heated to $\sim$300°C under high vacuum ($P \leq 1.0 \times 10^{-8} mbar$) for deposition and afterwards the sample was loaded back into UHV for STM measurements (**method 2**). In all STM images, the applied voltage is sample biased therefore a negative/positive bias represents the filled/empty states of the surface, respectively. STM measurements were carried out at room temperature.

4.2 Results & Discussion

Graphitization of SiC is one of the most reliable fabrication techniques for graphene growth since SiC is already a semiconducting substrate and there is no transfer process involved for the graphene layer itself. The graphene layer forms atop a $6\sqrt{3} \times 6\sqrt{3}R30°$ (hereafter referred to as $6\sqrt{3}$) reconstruction which has been previously studied.[81,82] Many models for the $6\sqrt{3}$ reconstruction have been proposed but it is still not absolutely known. The $6\sqrt{3}$ reconstruction acts as a buffer layer between graphene and the bulk SiC crystal and the monolayer of graphene only interacts with the $6\sqrt{3}$ via van der Waals interactions. A schematic of graphene is shown in Figure 4.3a and a side-view of graphene atop the $6\sqrt{3}$ reconstruction is shown in Figure 4.3b and the corresponding STM image is shown in Figure 4.3c. In the STM image, the underlying $6\sqrt{3}$ surface can be seen as a bright hexagonal superstructure where the small hexagonal structure is graphene.

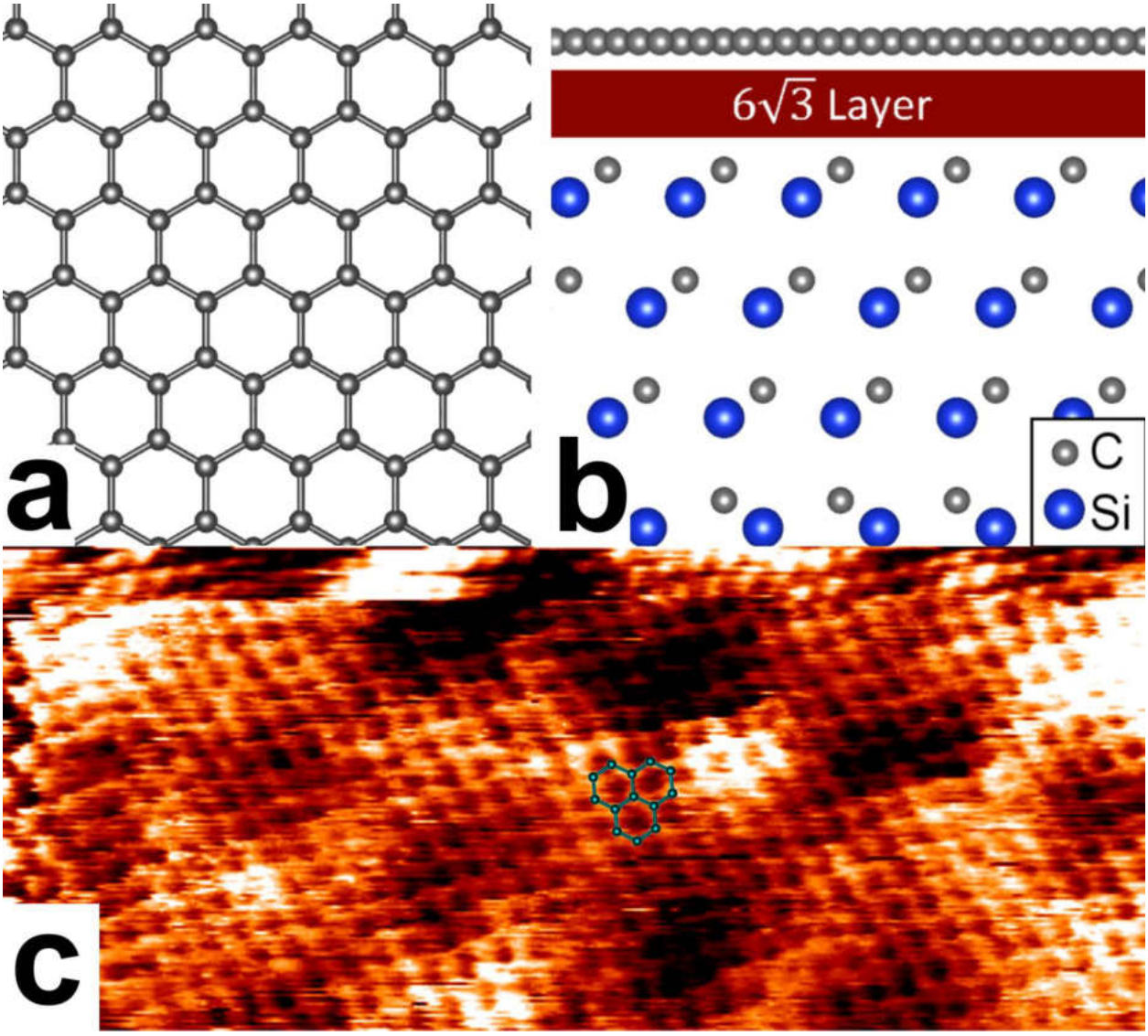

Figure 4. 3 (a) Schematic of graphene. (b) Side-view schematic showing graphene atop the $6\sqrt{3}$ buffer layer on a SiC substrate. (c) $10\,nm \times 3.75\,nm$ STM image of graphene over $(6\sqrt{3})$ reconstruction. $V = -0.774\,V, I = 0.827\,nA$.

Figure 4.4a shows a high-resolution STM image of graphene and one can clearly see the rings of carbon. Once the clean graphene surface was confirmed by STM measurements, Zn-Pc molecules were subsequently deposited. Whether Zn-Pc was deposited via method 1 or method 2, the amount of stable coverage (in monolayers (ML)) was in the average range of $0.00125\,ML$ to $0.005\,ML$ and both methods produced identical types of molecule coverage. In

the results below, method 1 was used to obtain Zn-Pc molecules on the surface. STM measurements (not shown) performed directly after deposition had a very amorphous and unstable surface configuration. The sample was subsequently heated to $< 200℃$ under UHV for a period of 1 minute in order to provide thermal energy for rearrangement of the Zn-Pc molecules.

In Figure 4.4b, two Zn-Pc molecules can be seen in the lower right hand corner and Figure 4.4c shows a higher quality image of the adsorbed Zn-Pc molecules. Line scans from Figure 4.4c (shown to the right of 4.4c) clearly show that the Zn-Pc molecules exhibit a dip (red arrow) in the center of the molecule and the adsorbed Zn-Pc molecule has an overall donut-like structure. This means that the core complex with the Zn atom has very minimal contribution to the filled states and the delocalized π-orbitals of the phthalocyanine structure are the main contribution to the filled states. The line scans also shows that the measured height of the Zn-Pc molecule is $\sim 0.4\ nm$ above the graphene surface as well as the diameter of the molecule is $\sim 1.8\ nm$. Since the Zn-Pc molecule is lying flat on the surface, one can infer that the π-π interactions between the molecule and the graphene surface is aiding in anchoring the molecule on the surface. However, due to the low surface coverage of the Zn-Pc molecules, it is easy to speculate that these molecules are extremely mobile at room temperature and may have a low vaporization pressure under vacuum. One can further speculate that the molecules that are stable on the surface may have adsorbed on defect sites in the graphene lattice however *ab-initio* calculations are needed to investigate further.

STS measurements were carried out with a lock-in amplifier in order to directly measure the first derivative of the $I(V)$ curve and then normalized to yield LDOS curves (see Figure 4.5a). The LDOS curves measured on graphene exhibit a dip at $0.42\ eV$ below the Fermi energy which is attributed to the Dirac point and is comparable to LDOS curves reported in literature.[83,84] The LDOS results obtained show clear shifts in the Dirac point for the edge and inner-core of the Zn-Pc molecule (see Figure 4.5b). Near the edge of the Zn-Pc molecule, the Dirac point shifts to $0.40\ eV$ below the Fermi level which correlates to a slight p-doping of the graphene states. LDOS curves measured on the inner-core of the Zn-Pc molecule exhibit a shift to $0.48\ eV$ below the Fermi level which correlates to a n-doping of the graphene states. Similar doping of monolayer graphene has been reported for various other molecules such as 4-amino-TEMPO by Choi *et al.* and PTCDA.[85] In order to gain further insight to the localized doping effects, density functional theory calculations are needed.

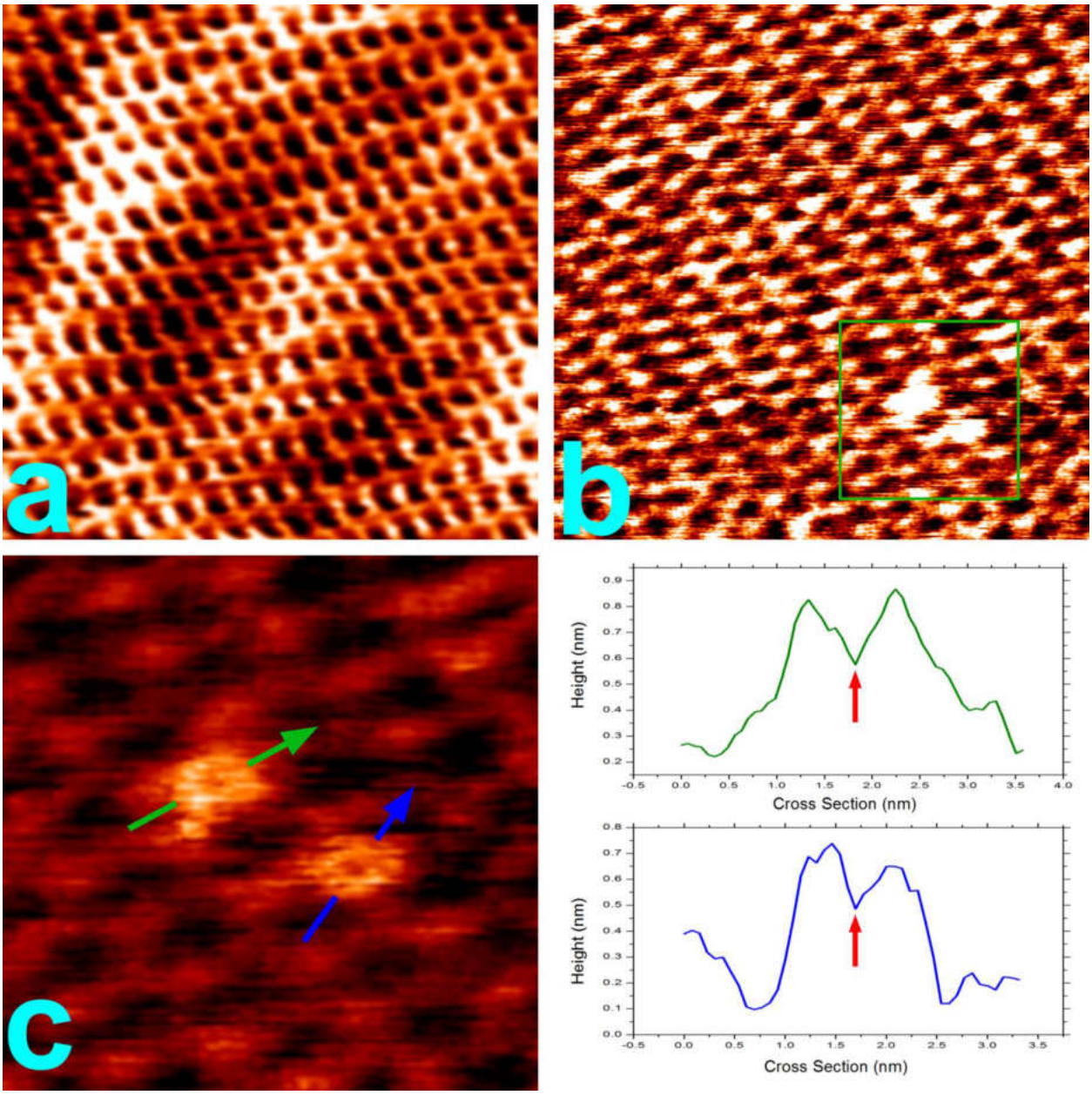

Figure 4. 4 (a) $5\ nm \times 5\ nm$ STM image of graphene over $\left(6\sqrt{3}\right)$ reconstruction $V = -0.606\ V$, $I = 0.508\ nA$. (b) $25\ nm \times 25\ nm$ STM image of Zn-Pc molecules on graphene $V = -0.929\ V$, $I = 0.777\ nA$. (c) $9\ nm \times 9\ nm$ STM image of highlighted region in (b), $V = -0.929\ V$, $I = 0.777\ nA$ and respective line scans across each of the Zn-Pc molecules.

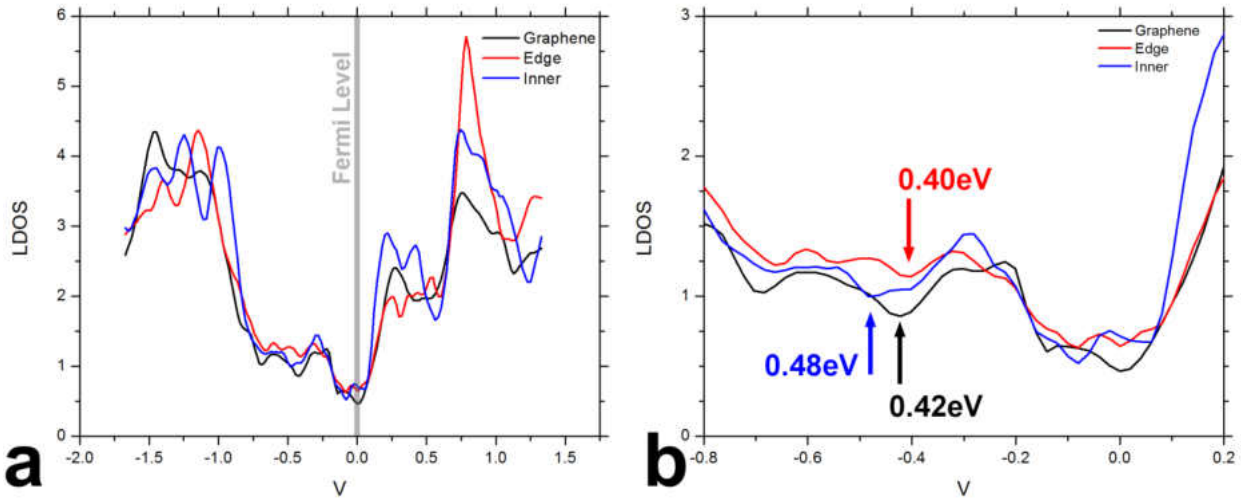

Figure 4. 5 (a) LDOS comparison of the graphene surface, edge of the Zn-Pc molecule, inner-core of the Zn-Pc molecule. (b) Section of the same LDOS curves in (a), near the Dirac point $\sim 0.42\ eV$. Clear shifts of the Dirac point near the (edge/inner-core) of the Zn-Pc molecule are evidence of (n-doping/p-doping), respectively.

4.3: Conclusion

STM measurements showed that Zn-Pc molecules were successfully adsorbed on epitaxially grown graphene on SiC(0001) and they lay parallel to the surface. The surface coverage in very small and it was very common to see only a few Zn-Pc molecules over a $1000\ nm^2$ region. STS measurements specifically showed shifts in the Dirac energy that can be attributed to localized doping effects caused by the presence of the Zn-Pc molecule. A uniform lamellae of this type of molecule would be able to alter the electronic structure of graphene enough to realize non-substitutional doping and functionalization of graphene.

CHAPTER V

IRIDIUM ON SILICON

Although there is extensive literature for most metal/silicon systems with various motivations, techniques and conclusions, it seems that Iridium (Ir) growth on silicon (Si) surfaces have not been studied with scanning tunneling microscopy/spectroscopy (STM/STS). Until our investigations, iridium silicides have only been studied in bulk phases and little was known of the initial growth of iridium on Si surfaces. Therefore, the work presented in this chapter fills an essential gap in our understanding of this important transition metal–silicon interface.

Iridium-silicides have three known crystal phases, which can be grown selectively in the sense that each silicide phase grows in a specific temperature range and only one silicide phase grows at a given temperature. The samples annealed below 410°C show no sign of crystallization. If the annealing temperature is between 410°C and 660°C, then a semi-amorphous and semi-conducting Ir_3Si_5 phase forms. The metallic IrSi phase forms when the annealing temperature is kept between 660-720°C. Above 720°C, the IrSi phase disappears and then if the annealing temperature reaches 1080°C, then the metallic $IrSi_3$ phase forms.[86,87] Therefore, it is vital to know how Ir grows on various surfaces of Si starting at sub-monolayer coverage to one or two monolayer coverage. This chapter covers our investigations of Ir on two different cuts of silicon, Si(111) and Si(100).[88,89]

5.1: Experimental-Si(111)

The Si(111) samples used in the STM experiments were cut from nominally flat $76.2\ mm \times 0.38\ mm$, single side-polished n-type (phosphorous doped) wafers purchased from Goodfellow. The samples were mounted on molybdenum holders and contact of the samples to any other metal during preparation and experiment was carefully avoided. The STM/STS studies have been performed by using an ultra-high vacuum (UHV with a base pressure $< 2 \times 10^{-10} mbar$) system equipped with an Omicron variable temperature STM and an LK technologies RVL2000 LEED–Auger system. Before introducing Si(111) samples in to the UHV chamber, samples were washed with isopropanol and dried under the flow of nitrogen gas. Si(111) samples were degassed extensively and then flash-annealed at $1250℃$ to obtain the Si(111)-7×7 reconstructed surface. The sample temperature was measured with a pyrometer. The quality of the clean Si(111) samples was confirmed both with LEED and STM prior to Ir deposition. Ir was deposited over the clean Si(111)-7×7 surface from a current heated Ir wire (99.9%) with a standard deposition rate of $2.8 \times 10^{-4}\ nm/s$. All the STM experiments were performed at room temperature. I–V curves measured at all points of the image while measuring high resolution STM images of the surface. The measured I–V curves were then averaged. The local density of states curves $\left(LDOS = \frac{dI}{dV}\left|\frac{V}{I}\right|\right)$ were calculated out of the I–V curves.

5.2: Results and Discussion-Si(111)

Figure 5.1 shows an STM image and a LEED intensity image of the clean Si(111)-7×7 surface. After confirming the quality of the sample both with STM and LEED, $0.25\,ML$ (monolayer) of Ir was deposited. Due to the existence of the three known crystal phases or Ir-silicides, we anticipated that there may be more different phases for various temperatures.

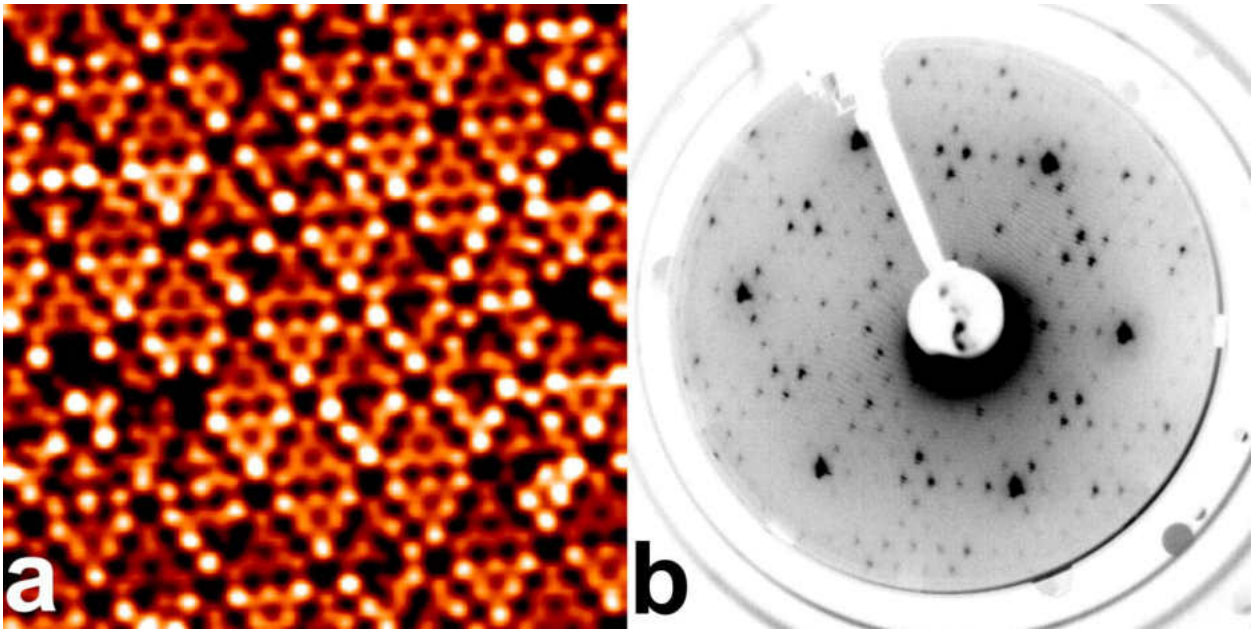

Figure 5. 1 (a) $16.75\ \text{nm} \times 16.75\ \text{nm}$ STM image of Si(111)- 7×7, $V = -1.709\,V, I = 0.398\,nA$. (b) LEED intensity image of same surface at $48\,eV$.

Therefore, we gradually increased the annealing temperature in a sequence up to 750℃. A sequence of LEED pattern measurements showed only the 1×1 pattern of Si(111) for a temperature range of ~ 350℃ to 650℃ (see Figure 5.2a). A new surface reconstruction was observed after the sample was annealed at 750℃ as shown in Figure 5.2b. The new LEED pattern was determined to be $\sqrt{7} \times \sqrt{7}\,R19.1°$ (hereafter as $\sqrt{7} \times \sqrt{7}$) and was confirmed using the LEEDPAT3.0 software package. The domains on the surface contained a $\sqrt{7} \times \sqrt{7}$ superlattice that is rotated $19.1°$ with respect to the hexagonal unit cell (1×1) of the

substrate. At temperatures higher than $850℃$ the $\sqrt{7} \times \sqrt{7}$ reconstruction starts to disappear and when the sample is annealed at $1250℃$ the surface remains with 7×7 and 1×1 domains.

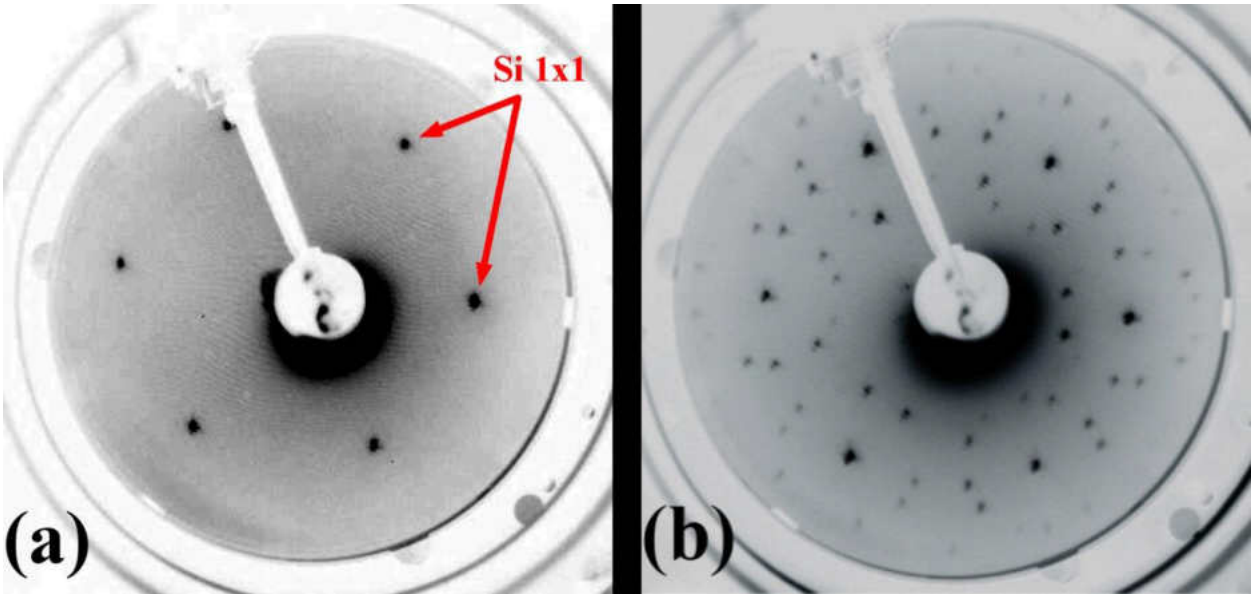

Figure 5. 2 LEED pattern sequence after annealing at: (a) $\sim 350℃ - 650℃$ showing only a Si 1×1 pattern, (b) $\sim 750℃$ with $\sqrt{7} \times \sqrt{7}\, R19.1°$ pattern.

A typical large scale STM image of the $\sqrt{7} \times \sqrt{7}$ surface is shown in Figure 5.3a and a closer look into the domain boundary clearly depicts the $19.1°$ rotation (Figure 5.3b), further confirming the LEED pattern we observed. The clusters that make up the $\sqrt{7} \times \sqrt{7}$ domain are Ir-ring clusters, which will be discussed in detail later. Another important feature of the $\sqrt{7} \times \sqrt{7}$ domains is the existence of holes that can be seen between domains or in the domains themselves. The size of these holes range from a few nm^2 to tens of nm^2. Obtaining well resolved structures in the smaller holes was not possible but larger holes show the typical Si(111)-7×7 structure, shown in Figure 5.3c. The height difference between the hole and the surrounding $\sqrt{7} \times \sqrt{7}$ domain is about $0.025\, nm$ which shows that they are on the same terrace (see Figure 5.3d and 5.3e).

In order to find further correlation between 7×7 and $\sqrt{7} \times \sqrt{7}$ domains, the sample was annealed at $1250℃$. It was found that the $\sqrt{7} \times \sqrt{7}$ Ir-ring clusters coexist together with the '1×1' domains although the concentration of Ir at the surface decreases drastically, leaving isolated Ir-ring clusters (see Figure 5.4a and 5.4b). It is also important to note that the Ir-ring clusters exist exclusively on the '1×1' domains and not on the 7×7 domains that are present on the surface. It can also be seen that the 7×7 domains are primarily established at terrace steps.

To investigate the $\sqrt{7} \times \sqrt{7}$ domains further, high-resolution STM images were taken with a dual voltage scan mode: where for each line the forward (backward) scan imaged the filled (empty) states. This allows us to correlate filled- and empty-state images without having to worry about drift. In both STM images (Figure 5.4c and 5.4d), the white protrusions marked with the letter 'X' are the ring clusters forming on top of a fully grown $\sqrt{7} \times \sqrt{7}$ domain. The filled- and empty-states are taken over the exact same area. The empty-state image shows three dot-like protrusions inside each cluster. A similar structure has been observed on cobalt-modified Si(111) surfaces where the structure was referred to as a ring cluster.[90-92] According to this ring cluster model (see Figure 5.4e), the transition metal atoms substitute Si atoms in the top substrate layer. This leaves each metal atom surrounded by six Si atoms, three of which directly bind to the transition metal atom and are called bridging adatoms and the remaining three Si atoms are called the capping adatoms which bind to two bridging adatoms and one Si substrate atom. Furthermore, the capping adatoms are situated slightly higher than the bridging adatoms and the underlying Si substrate that includes the Ir atom. Therefore, we attribute the three dot-like protrusions to the capping adatoms.

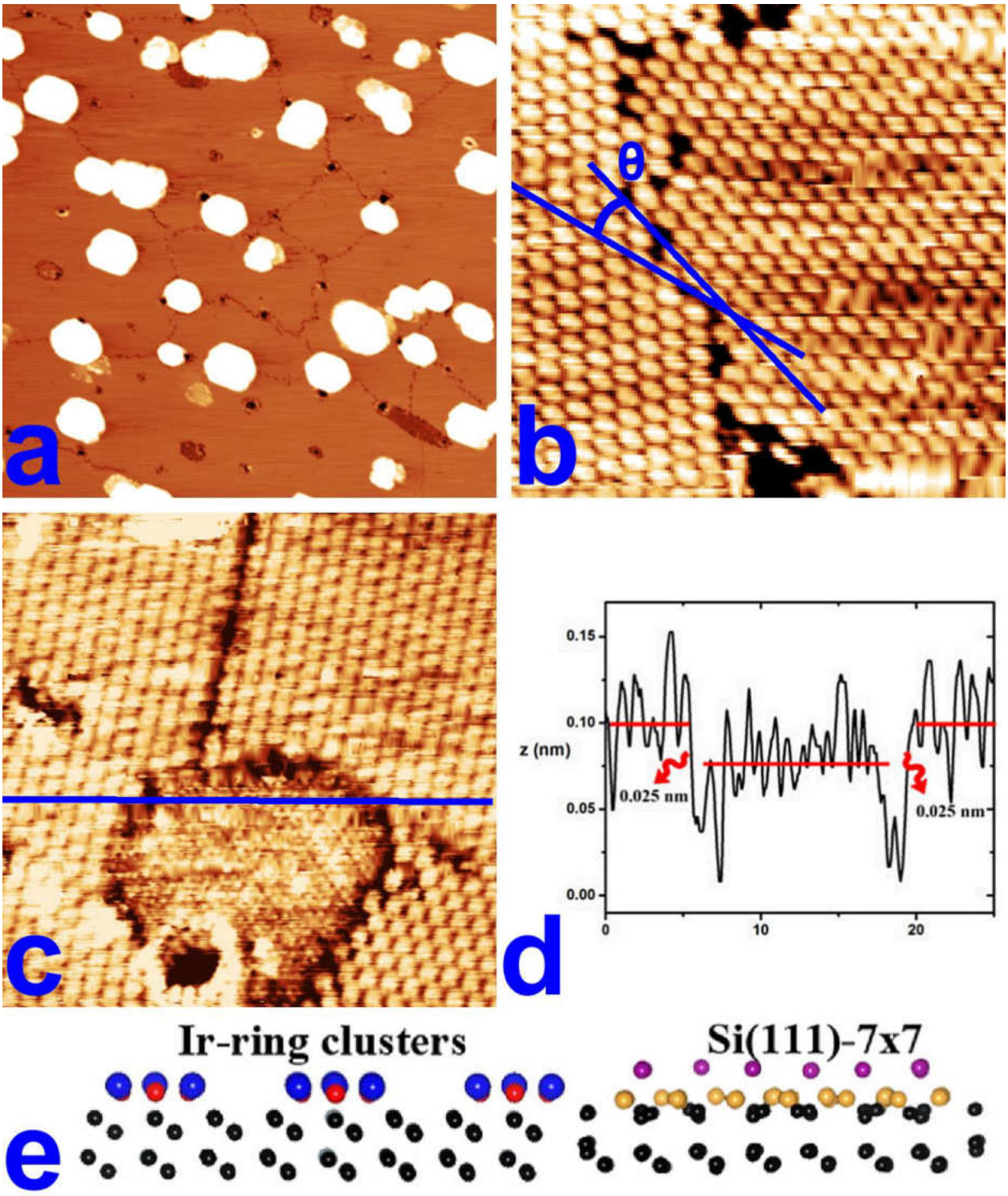

Figure 5. 3 (a) $180\ nm \times 180\ nm$ STM image of Si(111)-$\sqrt{7} \times \sqrt{7}R19.1°$ reconstructed surface, $V = -1.60\ V, I = 0.42\ nA$. (b) $18\ nm \times 18\ nm$ STM image of the $\sqrt{7} \times \sqrt{7}$ domain boundary, clearly showing a rotation of $\theta = 19.1°$, $V = -1.40\ V, I = 0.32\ nA$. (c) $25\ nm \times 25\ nm$ STM image of a large hole on surface with the line scan presented in (d). (e) Schematic showing Ir-ring clusters are on same terrace as Si(111)-7×7.

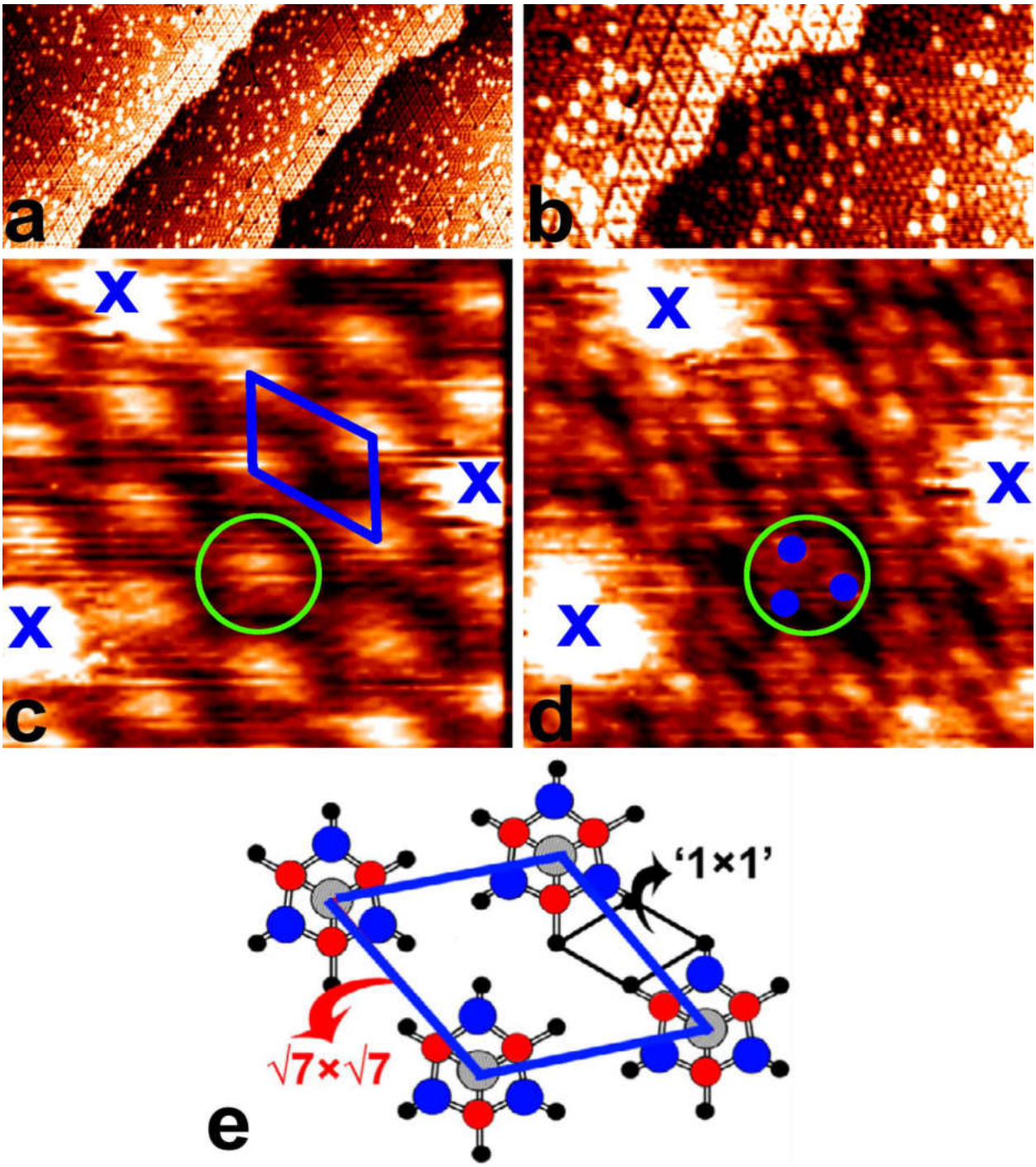

Figure 5. 4 (a) $100\ nm \times 50\ nm$ STM image of Ir modified Si(111) surface after annealing at ~1250℃, $V = -1.40\ V, I = 0.25\ nA$. (b) $40\ nm \times 20\ nm$ STM image of same surface showing domains of Ir-silicide ring clusters, $V = -1.60\ V, I = 0.25\ nA$. (c,d) $4.5\ nm \times 4.5\ nm$ STM images taken with dual voltage scan with (c) $V = -1.60\ V$ and (d) $V = 1.20\ V$ and $I = 0.42\ nA$ for both. The green circles indicate the same ring cluster and the blue dots in (d) indicate the capping adatoms. (e) Schematic of Ir-ring cluster with blue and red dots representing the capping and bridging adatoms, respectively.

Ir is a 5d metal and has a larger bonding radius than the 3d metal Co. The larger atomic radius can modify the atomic positions of a ring cluster in such a way that can make bridging adatoms less prone to tunneling; hence they show up darker in the STM image. On the other hand, in the filled-state STM image, the ring cluster appears as a single protrusion indicating that the filled-states must have significant contribution from the Ir atom at the center of the ring cluster.

Having elucidated the atomic structure of the Ir/Si(111) system by STM and LEED measurements, we now turn to the electronic structure of the surface. Figure 5.5a shows LDOS data obtained for the clean Si(111)-7×7 surface. The presented LDOS curved is similar to that in previously published results.[93,94] Following the literature, the filled states located at $-1.5\ V$ and $-0.7\ V$ are attributed to the corner holes and rest atoms, respectively The empty states at $0.8\ V$ and $1.3\ V$ are assigned to adatoms and adatom backbonds, respectively. Futhermore, there is the adatom state that crosses the Fermi level, making the Si(111)-7×7 surface metallic.

The LDOS curves measured on the '1×1' and $\sqrt{7} \times \sqrt{7}$ domains exhibit a marked change from that of the clean Si(111) LDOS curve. In Figure 5.5b, we observe two main features located at $0.3\ eV$ below and $0.8\ eV$ above the Fermi level. It is possible to used filled- and empty-state STM images like the ones presented in Figure 5.4(c,d) to explain the origin of these states. Working on this basis, we determined that the state located at $0.8\ eV$ above the Fermi level originates from the capping adatoms of the ring clusters and similarly, we determined that the state $0.3\ eV$ below the Fermi level carries a significant contribution from the Ir atom

together with the Si adatoms of the ring cluster. The LDOS curve measured the '1×1' domain shows a state located about $0.5\ eV$ below the Fermi level. In addition to that, there are multiple states that occupy the filled states. By comparing Fiugre 5.4b and 5.4c, one can argue that the filled state located at $0.3\ eV$ below the Fermi level observed on the $\sqrt{7} \times \sqrt{7}$ domain carries some contribution from the underlyind adatoms of the '1×1' domain. In order to gain further knowledge of Ir-silicides and explore other possible structures, we turn to another cut of the Si crystal, Si(100).

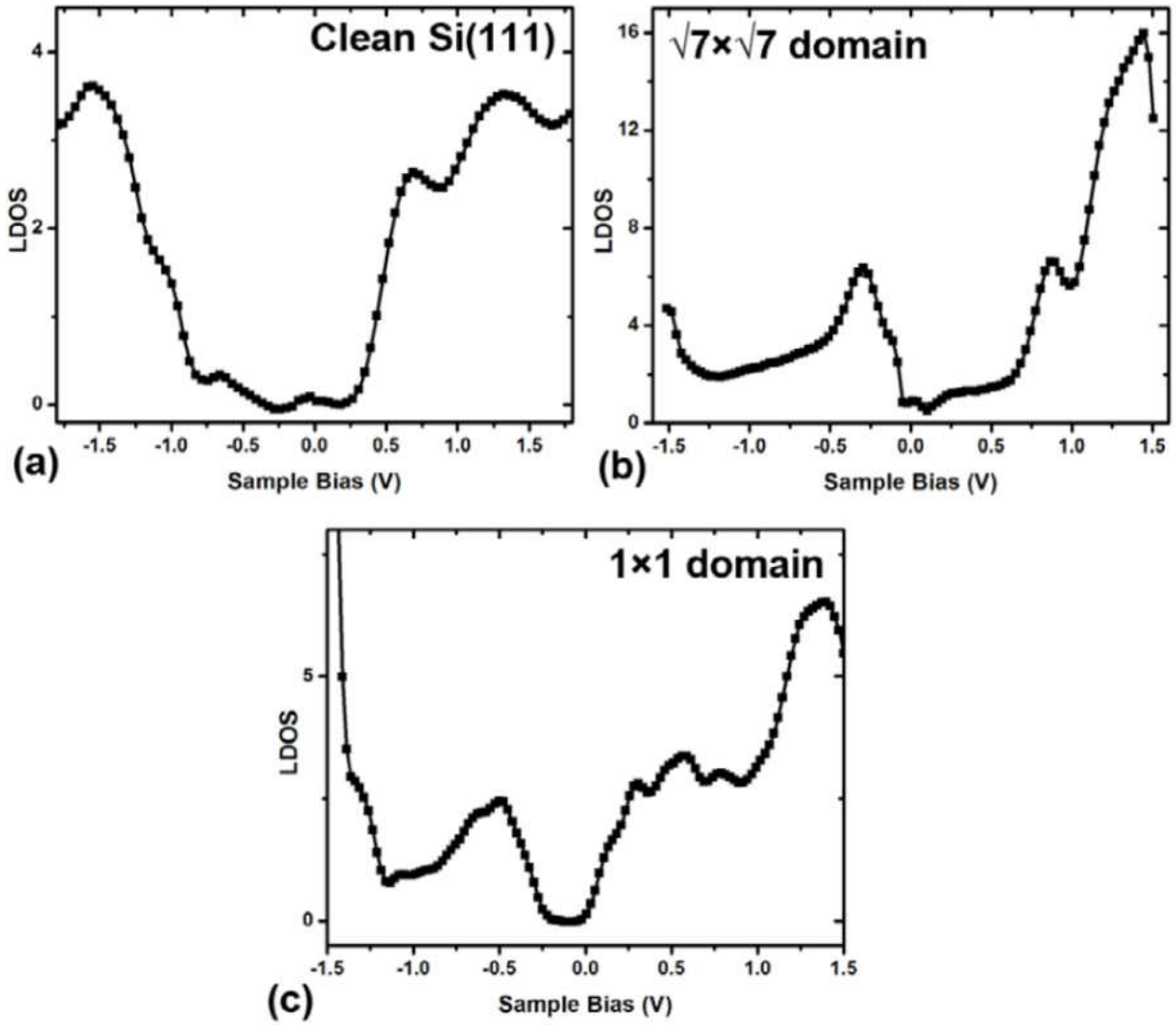

Figure 5. 5 LDOS curves measured on (a) a clean Si(111)-7 × 7 surface, (b) $\sqrt{7} \times \sqrt{7}$ domain, and (c) '1×1' domain.

5.3: Experimental-Si(100)

The Si(100) samples used in the STM experiments were cut from nominally flat $76.2\ mm \times 0.38\ mm$, single side-polished n-type (phosphorous doped) wafers purchased from Goodfellow. Sample preparation methods and UHV equipment were similar to that used on Si(111). Si(100) samples were degassed extensively and then flash-annealed at $1250℃$ to obtain the Si(100)-2×1 reconstructed surface. The quality of the clean Si(100) samples was

confirmed both with LEED and STM prior to Ir deposition. Ir was deposited over the clean Si(100)-2×1 surface from a current heated Ir wire (99.9%) with a standard deposition rate of $2.8 \times 10^{-4}\, nm/s$. All the STM experiments were performed at room temperature and Ir coverage was measured and calibrated with the help of Auger spectroscopy.

5.4: Results and Discussion-Si(100)

Figure 5.6a shows the LEED intensity image of Si(100)-2×1 reconstructed surface, prior to Ir deposition. After the deposition of Ir, we followed the same annealing method as performed on Si(111) by annealing at various temperatures to see if there would be different phases of Ir-silicides on the surface. The LEED intensity images shown in Figures 5.6(b-e) were measured after the sample was annealed at $700℃$, $800℃$, $900℃$, and $1000℃$, respectively. The $p(2 \times 2)$ pattern in Figure 5.6b deteriorates after annealing at higher temperatures. Once the sample was annealed at $1250℃$, the characteristic 2×1 pattern reappeared indicating that a clean Si(100) surface had returned. The quality of the surface was confirmed by LEED and STM, seen in Figure 5.7(a,b). However, as one can see, the surface has a high density of vacancy line defects (VLDs). These VLDs are attributed to the miniscule amount of Ir in the sub-surface layers.[95]

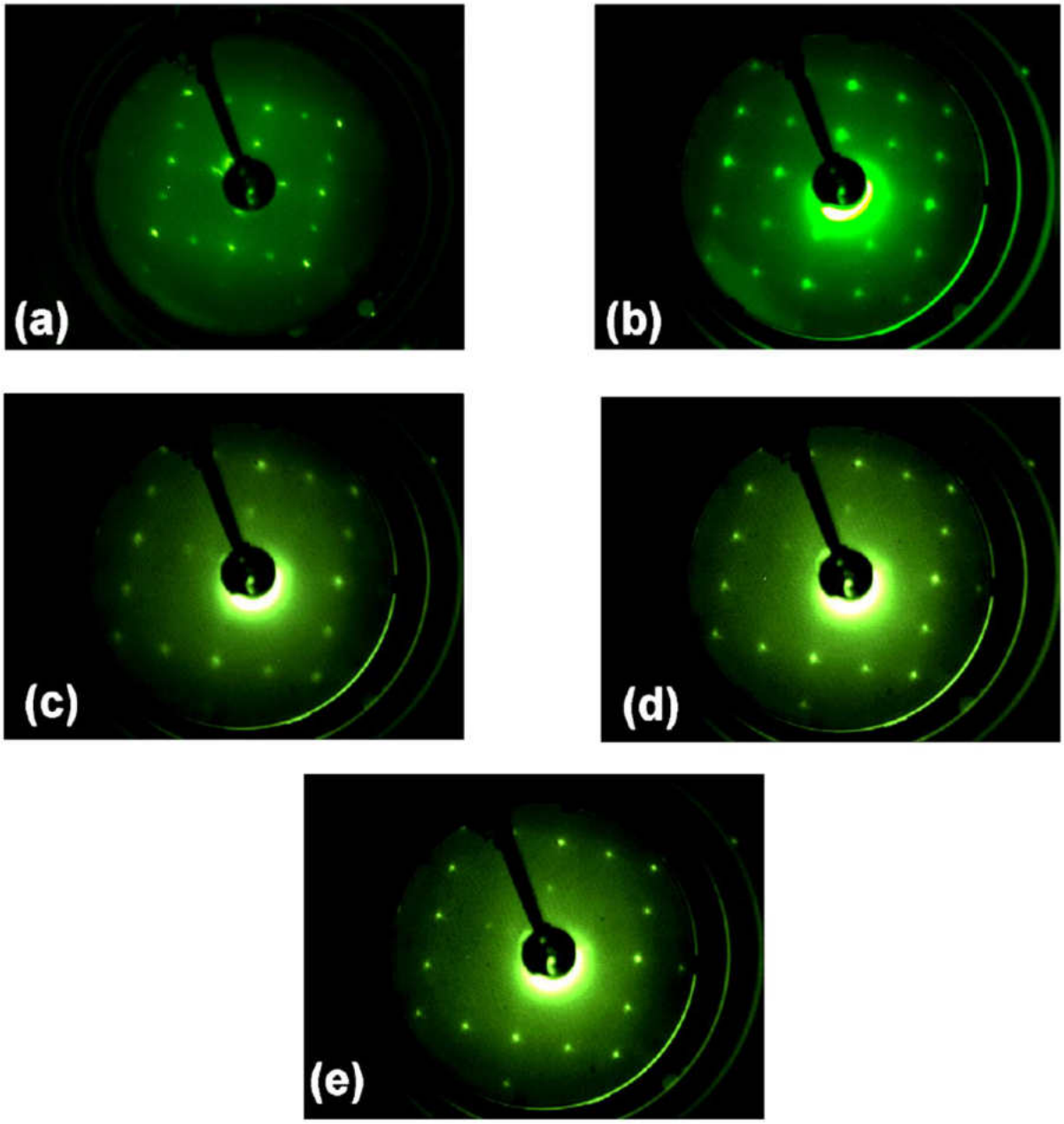

Figure 5. 6 LEED intensity images of: (a) Clean Si(100)-2×1 reconstructed surface, (b) Ir-modified Si(100) surface with a $p(2 \times 2)$ pattern, (c,d,e) Surface after annealing at 800℃, 900℃, and 1000℃, respectively. The electron energy for all LEED images is 49 eV.

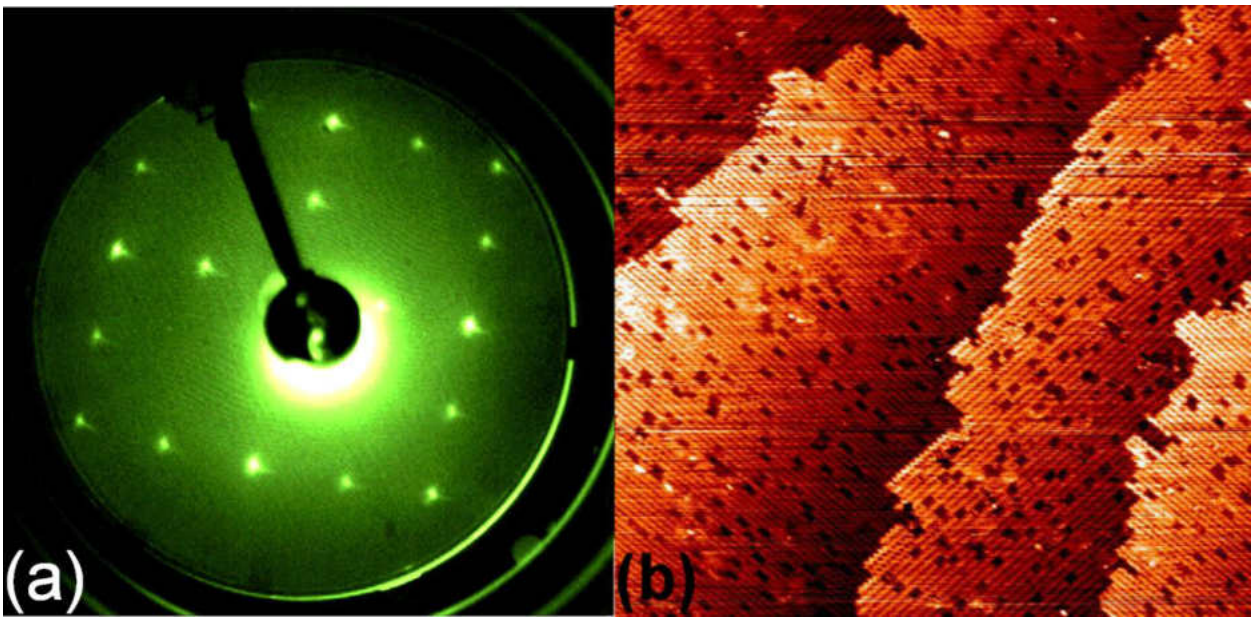

Figure 5. 7 (a) LEED intensity image showing Si(100)-2×1 returned after the Ir-modified sample was annealed at $1250℃$. The electron energy is 49eV. (b) $75\ nm \times 75\ nm$ STM image of the sample after the LEED image was taken, $V = -1.75\ V, I = 0.42\ nA$.

Once the transition from $p(2 \times 2)$ to 2×1 occurs, annealing the sample at $700℃$ does not bring back the $p(2 \times 2)$ pattern. The permanent loss of the $p(2 \times 2)$ domains is attributed to the diffusion of Ir atoms into the build of the silicon crystal. However, it is possible that some of the Ir atoms of the surface were evaporated back into the vacuum. In order to show that the disappearance of the $p(2 \times 2)$ pattern is due to Ir deficiency near the surface, we evaporated one more monolayer of Ir over the same surface. LEED and STM measurements confirmed that the $p(2 \times 2)$ pattern returned. Figure 5.8(a-c) shows two STM images of the $p(2 \times 2)$ surface. The surface consists of relatively small, irregular-shaped Ir-silicide terraces. The most striking feature of these terraces is that there are rows that stretch along [110] directions similar to the dimer rows of clean Si(100).[96] This suggests that the morphology of the Si(100) surface directly influences the structure of these Ir-silicide terraces. Figure 5.8d shows two line scans measured on boundaries that separate two Ir-silicide terraces that are aligned perpendicular (green

arrow) and parallel (blue arrow) to one another. As the graphs show, the terraces that are aligned perpendicular are at different heights indicating the presence of a step edge. On the other hand, the terraces aligned parallel are separated by a regular domain wall meaning that the terraces are at the same height.

In order to study the initial stages of growth of these Ir-silicide terraces and find the correlation between them and the Si(100) surface, we deposited $0.125\ ML$ of Ir. As before, the sample was annealed at $700℃$. Figure 5.9a shows a LEED intensity image of the surface measured after Ir deposition and in Figure 5.9b the line scan measured from (01) beam to the (21) beam shows a faint 2×2 peak. In the inset of Figure 5.9b, an STM image shows that there are Ir-silicide terrace islands amidst a wetting layer. The subsequent STM measurement, shown in Figure 5.10a, clearly demonstrates that the Ir-silicide terraces are aligned along the [110] direction of the silicon dimer rows. A high resolution STM image of the Si(100) wetting layer is shown in Figure 5.10b. The Ir modified Si(100) surface is full of VLDs and Figure 5.10c shows a line scan over one of these VLDs. The VLDs are a combination of one-dimer vacancy (1-DV) and two-dimer vacancy (2-DV) defects.[97,98] A schematic model of a VLD is presented in the inset of Figure 5.10c. The VLDs on the Ir modified Si(100) surface prefer to form on two neighboring dimer rows leading to 'coupled' VLDs. One such a structure is encircled in Figure 5.10b. Observation of these 'coupled' VLDs is in line with the previously claimed short-range attractive interaction between VLDs.[99]

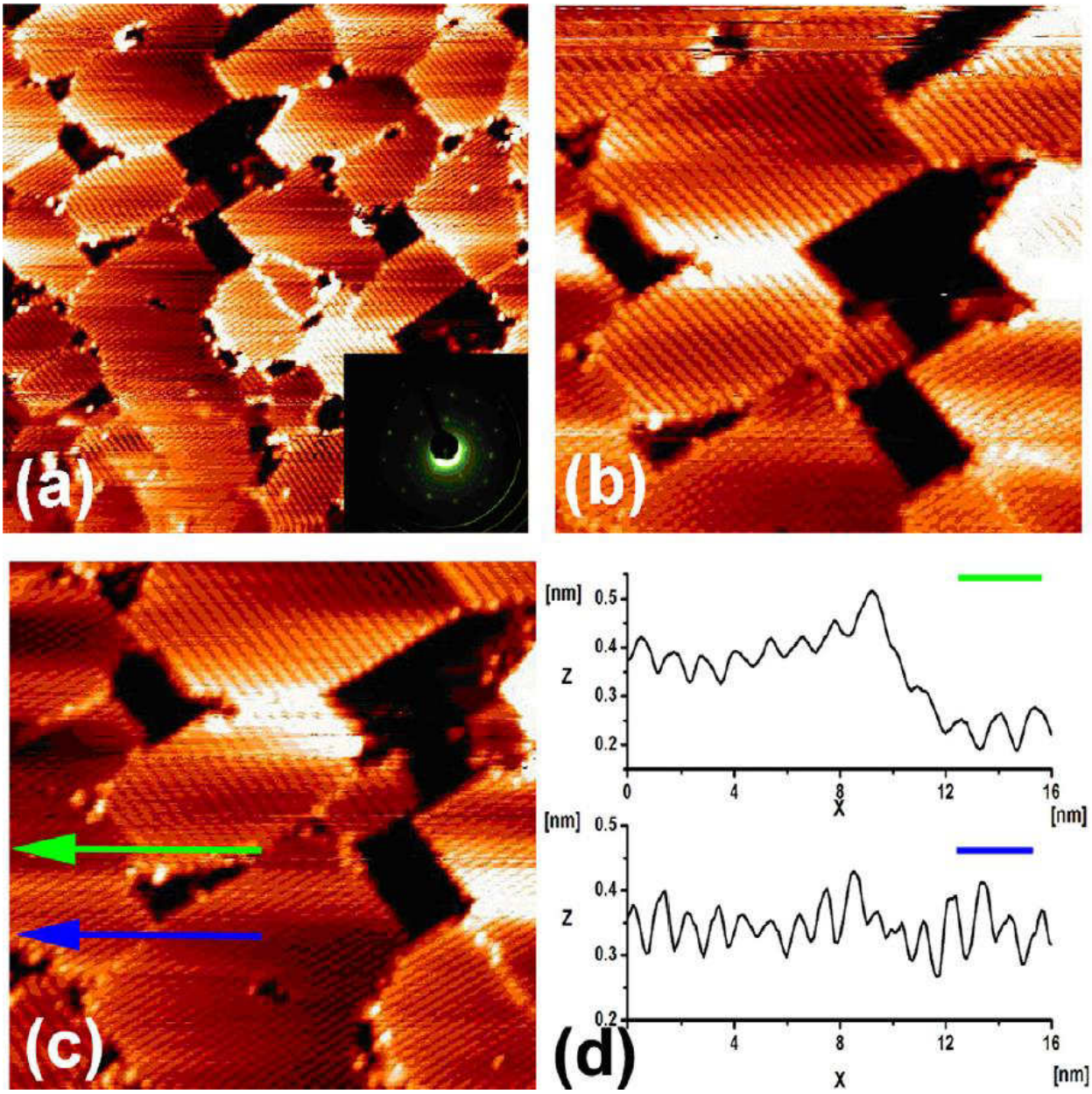

Figure 5. 8 (a) $80\ nm \times 80\ nm$ STM image of the Ir modified Si surface, $V = -1.55\ V, I = 0.44\ nA$. Inset is the LEED intensity image of such a surface with the electron energy of 49 eV. (b) $40\ nm \times 40\ nm$ STM image of the same surface, $V = -1.54\ V, I = 0.44\ nA$. (c) $40\ nm \times 40\ nm$ STM image of the same surface, $V = -1.54\ V, I = 0.44\ nA$. (d) Line scans measured over the green and blue arrows in (c). The green (blue) arrow goes over a boundary that separates two Ir-silicide terraces rotated $90°$ $(0°)$.

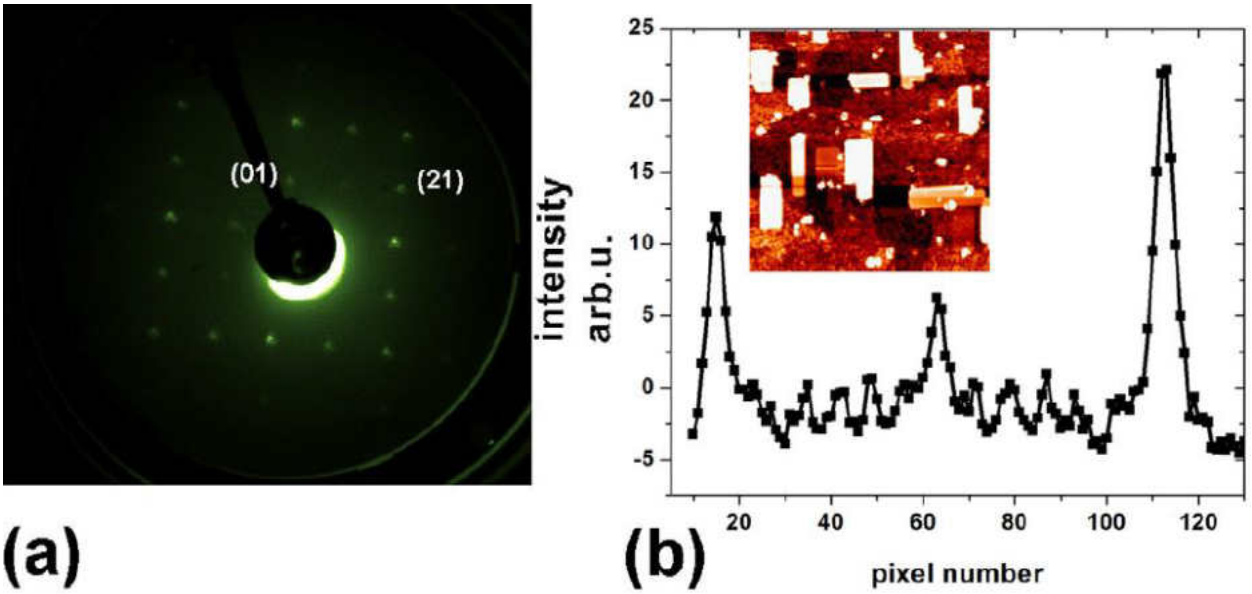

Figure 5. 9 (a) LEED intensity image after $0.125\ ML$ of Ir deposition and annealing at $700℃$. (b) Line scan of LEED image from (01) beam to (21) beam. The electron energy for the LEED pattern is 49 eV. Inset is the corresponding large-scale STM image of the surface.

A high resolution, 3-D STM image of an Ir-silicide terrace is present in Figure 5.11a. The terrace is made out what we call Ir-silicide nanowires. The lattice vector across the nanowires is approximately $0.7 \pm 0.1\ nm$ which is almost equal to the distance between two neighboring Si dimer rows ($\sim 0.75\ nm$) of a clean Si(100) surface. On the other hand, the length of the lattice vector along the nanowires is $0.9 \pm 0.1\ nm$, which is about two times longer that the distance between Si dimers ($\sim 0.38\ nm$). In addition to that, the line scans in Figure 5.11b(top) show that the nanowires are composed of asymmetric dimers. Based on this information, we propose a model for the Ir-silicide nanowires, shown in Figure 5.11b(middle). According to this model, Ir atoms replace ever other Si dimer. The taller part of a dimer is attributed to the Ir atom since large 5d orbitals of Ir atoms enable a higher tunneling rate which leads to a protrusion in the STM image. However, *ab-initio* calculations are needed to determine the exact nature of this structure.

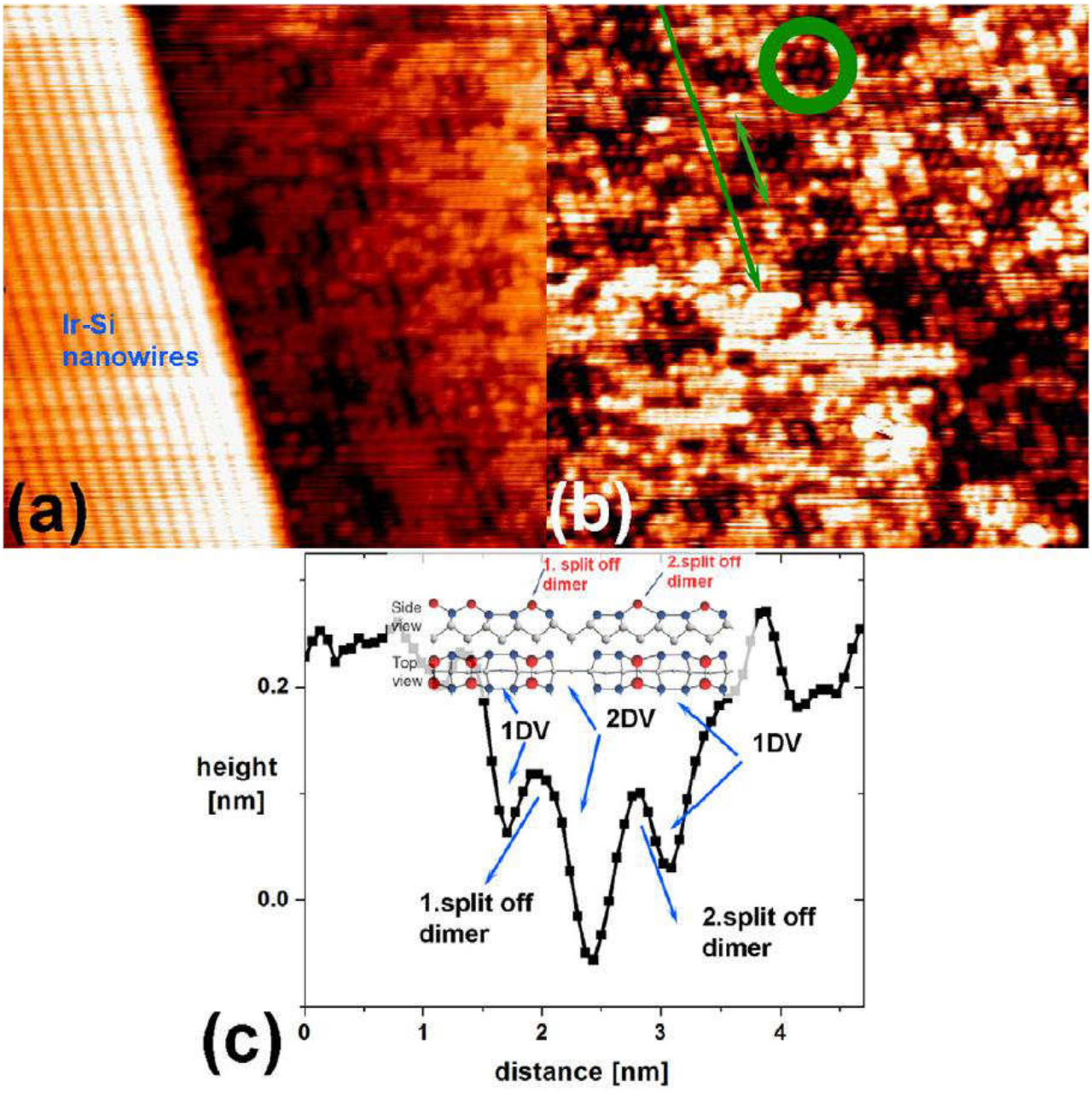

Figure 5. 10 (a) $25\ nm \times 25\ nm$ STM image showing both Ir-silicide terrace and Si(100) surface, $V = -1.0\ V, I = 0.5\ nA$. (b) $24\ nm \times 24\ nm$ STM image of the Ir modified Si(100) surface, $V = -1.0\ V, I = 0.5\ nA$. The longer arrows indicates both the direction of Ir-silicide nanowires and dimer rows of Si(100). (c) Line scan over the shorter arrow presented with a model of the Si(100) terrace.

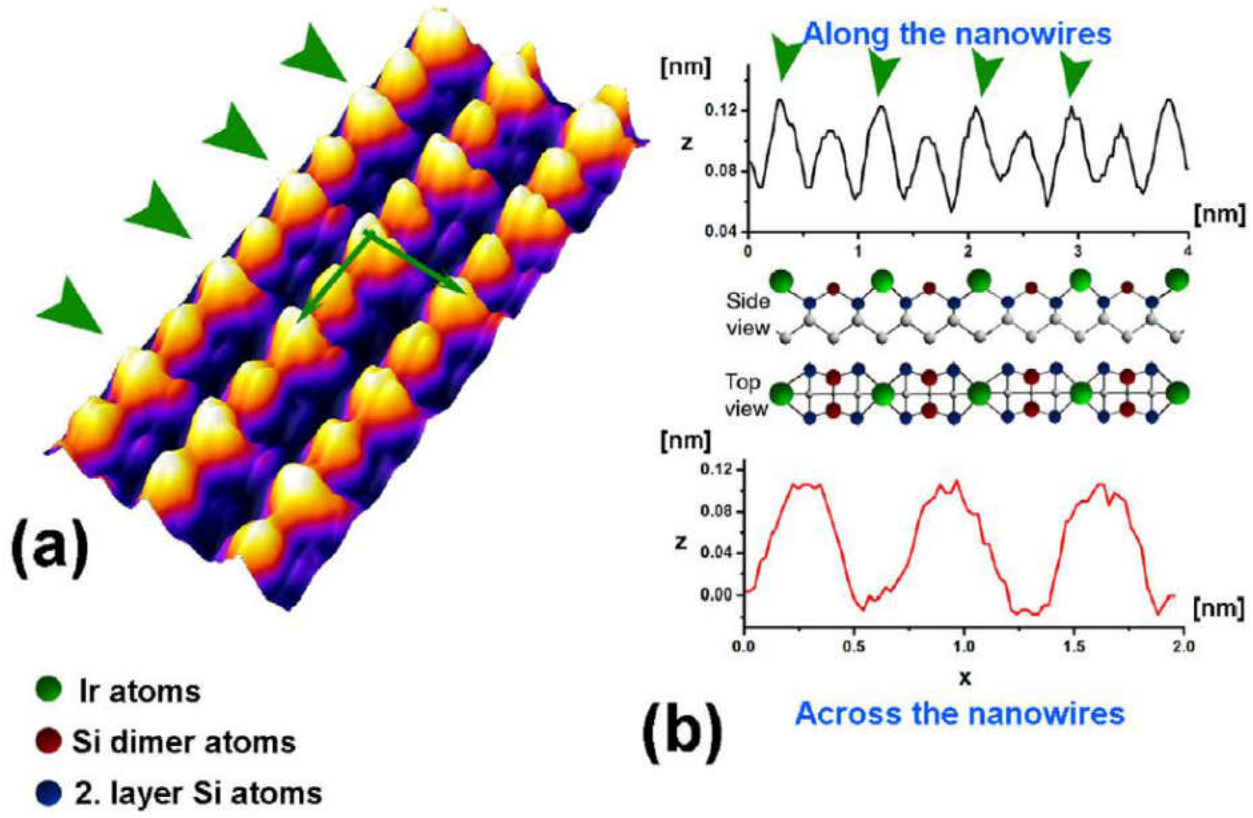

Figure 5. 11 (a) $4.5\ nm \times 2\ nm$ 3-D STM image of the Ir-silicide nanowires, $V = -1.0\ V, I = 0.5\ nA$. (b) Top (bottom) shows a line scan along (across) the nanowires. A schematic model for the Ir-silicide nanowires is presented between the line scans.

5.5 Conclusion

In conclusion, Ir-modified Si(111) and Si(100) surfaces were studied with LEED and STM to gain insight on the initial growth of Ir-silicides and their electronic behavior. The Ir-modified Si(111) surface exhibited a $\sqrt{7} \times \sqrt{7}$ domain formation in which we proposed that these domains consist of Ir-ring clusters. In each cluster, an Ir atom is surrounded by six silicon adatoms. LDOS measurements on the $\sqrt{7} \times \sqrt{7}$ domain showed peaks at $\sim 0.3\ eV$ below and $\sim 0.8\ eV$ above the Fermi level and when compared with filled- and empty-state STM images, these states were attributed to Ir atoms together with the Si adatoms of the ring cluster and capping adatoms, respectively.

The Ir-modified Si(100) surface yielded the formation of Ir-silicide nanowires that form at $\sim 700℃$. Once the sample was annealed at higher temperatures, a non-reversible transition was observed. This transition was attributed to the diffusion of Ir atoms into the bulk of the Si crystal. Deposition of more Ir reverses this transition and the $p(2 \times 2)$ domain reconstructs. The proposed model for the Ir-silicide nanowires shows that an Ir atom replaces every other Si dimer along the Si dimer rows of Si(100)-2×1.

CHAPTER VI

CONCLUSION

The presented dissertation focuses on two seemingly different topics, molecular films on graphene/graphite and metal induced changes in various cuts of silicon surfaces. However, both projects share an underlying theme: self-assembly. I believe that self-assembly is the answer for scaling down functional components in integrated circuits, increasing efficiency of electronic and photonic devices as well as reducing costs of consumer electronics. Since nature can rely on self-assembly, we just need to find recipes to create functional structures out of atoms and molecules.

Experiments performed on molecular lamellae and chains on highly ordered pyrolytic graphite in Chapter 2 served as inspiration to study the effects of molecular adsorption on the technologically relevant surface of graphene. The main motivation behind this project was to investigate whether it is possible to modify the electronic properties of graphene, especially around the Dirac point, by the physical adsorption of organic molecules. Such a system, with carefully designed organic molecules can be used in various applications such as harvesting solar energy or electronic sensors. For this project we chose Zn(II)-Phthalocyanine tetra sulfonic acid (Zn-Pc). STM measurements showed that a low coverage of Zn-Pc molecules were successfully adsorbed on epitaxially grown graphene on 6H-SiC(0001). Most importantly, LDOS measurements showed shifts in the Dirac point of graphene that correlate to localized n-doping

effects from the core of the Zn-Pc molecule and localized p-doping effects from the sulfonic acid groups on the edge of the molecule.

We also investigated Ir-modifed Si(111) and Si(001) surfaces. STM measurements showed that Ir-ring clusters form on the Si(111) surface. The ring clusters contains six silicon adatoms surrounding an Ir atom at the center. The clusters come together and form $\sqrt{7} \times \sqrt{7}$ domains on the surface. The surface has a band gap and by comparing filled and empty state STM images, we managed to assign the origins of the observed peaks in the LDOS measurements.

On the other hand, STM images measured on Ir-modified Si(001) surface showed that the surface hosts Ir-silicide nanowires. LEED images showed a $p(2 \times 2)$ intensity pattern after the deposition of Ir and subsequent annealing of the surface at $T \approx 750$℃. STM images of neighboring Ir-silicide domains as well as the wetting layer near the Ir-silicide wires suggest that the wires form along the dimer rows of Si(100)-2×1. A tentative model proposed for the Ir-silicide nanowires shows that an Ir atom replaces every other Si dimer. Our investigation on Ir-modified Si(001) surface is nowhere near completion and I believe that these initial studies will constitute a strong foundation to future work.

As it was said by Richard Feynman, "…'there is plenty of room at the bottom' –not just 'there is room at the bottom'."

REFERENCES

[1] Feynman, Richard. “There’s Plenty of Room at the Bottom." American Physical Society. California Institute of Technology. 29 December 1959. Lecture.

[2] Ito, T, and S Okazaki. “Pushing the Limits of Lithography.” Nature 406.6799 (2000): 1027–31.

[3] Oncel, Nuri et al. “Quantum Confinement Between Self-Organized Pt Nanowires on Ge(001).” Physical Review Letters 95.11 (2005): 116801.

[4] Baski, A. A., K. M. Jones, and K. M. Saoud. “STM Studies of 1-D Noble Metal Growth on Silicon.” Ultramicroscopy 86.1-2 (2001): 23–30.

[5] Ross, F., J. Tersoff, and R. Tromp. “Coarsening of Self-Assembled Ge Quantum Dots on Si(001).” Physical Review Letters 80.5 (1998): 984–987.

[6] Tao, Feng, Julie Goswami, and Steven L Bernasek. “Competition and Coadsorption of Di-Acids and Carboxylic Acid Solvents on HOPG.” J. Phys. Chem. B 110.39 (2006): 19562–9.

[7] Tao, Feng. “Nanoscale Surface Chemistry in Self- and Directed-Assembly of Organic Molecules on Solid Surfaces and Synthesis of Nanostructured Organic Architectures.” Pure and Applied Chemistry 80.1 (2008): 45–57.

[8] Phillips, Tamsin K et al. “Adsorption of Aldehydes on a Graphite Substrate : Combined Thermodynamic Study of C6 - C13 Homologues with a Structural and Dynamical Study of Dodecanal.” (2010): 6027–6034.

[9] Beggan, J P et al. “Self-Assembly of Ni(II) Porphine Molecules on the Ag/Si(111)-(√3 x √3R30) Surface Studied by STM/STS and LEED.” Journal of Physics: Condensed Matter 20.1 (2008): 015003.

[10] Barth, Johannes V, Giovanni Costantini, and Klaus Kern. “Engineering Atomic and Molecular Nanostructures at Surfaces.” Nature 437.7059 (2005): 671–9.

[11] Erben, C.; Will, S.; Kadish, K. M. Metallocorroles: Molecular Structure, Spectroscopy and Electronic States, ch. 12 in The Porphyrin Hanbook, Kadish KM, Smith KM, Guilard R. Eds. Academic Press, 2000.

[12] Lee, Sang-kyung, and Ichiro Okura. “Optical Sensor for Oxygen Using a Porphyrin-Doped Sol – Gel Glass.” 122.January (1997): 81–84.

[13] Campbell, Wayne M. et al. “Porphyrins as Light Harvesters in the Dye-Sensitised TiO2 Solar Cell.” Coordination Chemistry Reviews 248.13-14 (2004): 1363–1379.

[14] Campbell, Wayne M et al. “Highly Efficient Porphyrin Sensitizers for Dye-Sensitized Solar Cells.” 36.3 (2007): 11760–11762.

[15] Panchmatia, Pooja M., Biplab Sanyal, and Peter M. Oppeneer. “GGA+U Modeling of Structural, Electronic, and Magnetic Properties of Iron Porphyrin-Type Molecules.” Chemical Physics 343.1 (2008): 47–60.

[16] Machado, Guilherme Sippel et al. “Aluminosilicate Obtained by Sol–gel Process as Support for an Anionic Iron Porphyrin: Development of a Selective and Reusable Catalyst for Oxidation Reactions.” Colloids and Surfaces A: Physicochemical and Engineering Aspects 349.1-3 (2009): 162–169.

[17] Ambroise, Arounaguiry et al. “Design and Synthesis of Porphyrin-Based Optoelectronic Gates.” Chem. Mater. (2001): 1023–1034.

[18]Koo, Ja-Ryong et al. “Electrical Properties of Porphyrin-Based Switching Devices.” Thin Solid Films 438-439.03 (2003): 123–127.
[19]Elemans, J.a.a.W. et al. “Scanning Probe Studies of Porphyrin Assemblies and Their Supramolecular Manipulation at a Solid–Liquid Interface.” Advanced Materials 15.24 (2003): 2070–2073.
[20]Castro Neto, a. H. et al. “The Electronic Properties of Graphene.” Reviews of Modern Physics 81.1 (2009): 109–162.
[21]Zhang, Yuanbo et al. “Experimental Observation of the Quantum Hall Effect and Berry’s Phase in Graphene.” Nature 438.7065 (2005): 201–4.
[22]Novoselov, K S et al. “Two-Dimensional Gas of Massless Dirac Fermions in Graphene.” Nature 438.7065 (2005): 197–200.
[23]Novoselov, K S et al. “Electric Field Effect in Atomically Thin Carbon Films.” Science (New York, N.Y.) 306.5696 (2004): 666–9.
[24]Kedzierski, Jakub et al. “Epitaxial Graphene Transistors on SiC Substrates.” 55.8 (2008): 2078–2085.
[25]Substrates, Si-face et al. “Epitaxial-Graphene RF Field-Effect Transistors.” 30.6 (2009): 650–652.
[26]Huang, Bing et al. “Making a Field Effect Transistor on a Single Graphene Nanoribbon by Selective Doping.” Applied Physics Letters 91.25 (2007): 253122.
[27]Lherbier, Aurélien et al. “Charge Transport in Chemically Doped 2D Graphene.” Physical Review Letters 101.3 (2008): 036808.
[28]Boukhvalov, D. W., and M. I. Katsnelson. “Destruction of Graphene by Metal Adatoms.” Applied Physics Letters 95.2 (2009): 023109.
[29]Sun, J. T. et al. “Linear Tuning of Charge Carriers in Graphene by Organic Molecules and Charge-Transfer Complexes.” Physical Review B 81.15 (2010): 155403.
[30]Dubois, Emmanuel, and Guilhem Larrieu. “Low Schottky Barrier Source/drain for Advanced MOS Architecture: Device Design and Material Considerations.” Solid-State Electronics 46.7 (2002): 997–1004.
[31]Larrieu, G. et al. “Formation of Platinum-Based Silicide Contacts: Kinetics, Stoichiometry, and Current Drive Capabilities.” Journal of Applied Physics 94.12 (2003): 7801.
[32]W. Cabanski, R. Koch, H. Mainer, G. Paler, J. Wendler, J. Ziegler, K. Hofmann, K. Eberhardt, P. Daimel, U. Prechtl, K. Kapser, “AEG PtSi modules: a summary” Proc. SPIE. (1996): 2746.
[33]Czernick, H. Palm, W. Cabanski, M. Schulz, U. Suckow, “Infrared photoemission of holes from ultrathin (3–20 nm) Pt/Ir-compound silicide films into silicon” Appl. Phys. A 55 (1992): 180-191.
[34]B.-Y. Tsaur, M. M. Weeks, and P. W. Pellegrini, “Pt-Ir silicide Schottky-barrier IR detectors” IEEE Electron Device Lett. 9 (1988): 100.
[35]J. J. Chu, L. J. Chen, K. N. Tu, “Localized epitaxial growth of IrSi3 on (111) and (001) silicon” J. Appl. Phys. 63 (1988): 1163.
[36]T. L. Lin, C. W. Nieh, S. Hashimoto, Q.F. Xiao, “ Growth of IrSi3 by molecular beam epitaxy” Thin Solid Films 184 (1990): 343.
[37]D. A. Lange, G. A. Gibson, C. M. Falco, “Growth and structure of IrSi3 on Si(111)” J. Appl. Phys. 75 (1994): 2917.
[38]Almendra, A. Rodriguez, R. Rodriquez, S. N. Shamin, V. I. Aksenova, “The role of the Si 3s3d states in the bonding of iridium silicides (IrSi, Ir3Si5 and IrSi3)”J. of Phys. Cond. Matt. 14 (2002): 3599.
[39]V. Demuth, H. P. Strunk, D. Worle, C. Kumpf, E. Burkel, M. Schulz, “Formation of amorphous layers by solid-state reaction. from thin Ir films on Si(100)” Appl. Phys. A 68 (1999): 451.
[40]Y. P. Zhang, L. Yang, Y. H. Lai, G. Q. Xu, and X. S. Wang, “Self-assembly of one-dimensional molecular nanostructures on the Ge-covered Si(100) surface”Appl. Phys. Lett. 84 (2004): 401.

[41]H. Okino, I. Matsuda, R. Hobara, Y. Hosomura, S. Hasegawa, and P. A. Bennett, “In situ resistance measurements of epitaxial cobalt silicide nanowires on Si(110)” Appl. Phys. Lett. 86 (2005): 233108.
[42]Kida, H. Kajiyama, S. Heike, T. Hashizume, and K. Koike, “Self-organized growth of Fe nanowire array on H2O/Si(100)(2×n)” Appl. Phys. Lett. 75 (1999): 540.
[43]R. Losio, K. N. Altmann and F. J. Himpsel, “Continuous Transition from Two- to One-Dimensional States in Si(111)-(5×2)–Au” Phys. Rev. Lett. 85 (2000): 808.
[44]J. R. Ahn, H. W. Yeom, H. S. Yoon, and I. -W. Lyo, “Metal-Insulator Transition in Au Atomic Chains on Si with Two Proximal Bands” Phys. Rev. Lett. 91 (2003) 196403.
[45]J. H. G. Owen, K. Miki, and D. R. Bowler, “Self-assembled nanowires on semiconductor surfaces” J. Mater. Sci. 41 (2006): 4568.
[46]Y. Chen, D. A.A. Ohlberg, G. Mederios-Ribario, Y. A. Chang, and R. S. Williams, “Self-assembled growth of epitaxial erbium disilicide nanowires on silicon (001)” Appl. Phys. Lett. 76 (2000): 4004.
[47]Y. Chen, D. A.A. Ohlberg, and R. S. Williams, “Nanowires of four epitaxial hexagonal silicides grown on Si(001)” J. Appl. Phys. 91 (2002): 3213.
[48]J. Nogami, B. Z. Liu, M. V. Katkov, C. Ohbuchi, and N. O. Birge, “Self-assembled rare-earth silicide nanowires on Si(001)” Phys. Rev. B 63 (2001): 233305.
[49]O. Gurlu, O. A.O Adam, H. J.W. Zandvliet, and B. Poelsema, “Self-organized, one-dimensional Pt nanowires on Ge(001)” Appl. Phys. Lett. 83 (2003): 4610.
[50]J. Wang, M. Li, and E. I. Altman, “Scanning tunneling microscopy study of self-organized Au atomic chain growth on Ge(001)” Phys. Rev. B 70 (2004): 233312.
[51]Bardeen, J. “Physical Review Letters.” Physical Review Letters 6.2 (1961): 57–59.
[52]Chen, C. J., 1993, Introduction to Scanning Tunneling Microscopy (Oxford University Press, New York).
[53]Feenstra, R. M., et al. “Tunneling Spectroscopy of the Si(111)2x1 Surface.” Surface Science 181.1-2 (1987): 295-306.
[54]Tsuboi, Taiju, Yoko Wasai, and Nataliya Nabatova-Gabain. “Optical Constants of Platinum Octaethyl Porphyrin in Single-Layer Organic Light Emitting Diode Studied by Spectroscopic Ellipsometry.” Thin Solid Films 496.2 (2006): 674–678.
[55]Bansal, a.K. et al. “Absorption and Emission Spectroscopic Characterization of Platinum-Octaethyl-Porphyrin (PtOEP).” Chemical Physics 330.1-2 (2006): 118–129.
[56]J. Everse, K. D. Vandegriff and R. M. Wislow, Hemoglobins Academic Press, San Diego. (1994).
[57]E. F. Johnson, M. R. Waterman, Cytochrome P450 Academic Press, San Diego. (1996).
[58]Huber, Valerie, Marina Lysetska, and Frank Würthner. “Self-Assembled Single- and Double-Stack Pi-Aggregates of Chlorophyll Derivatives on Highly Ordered Pyrolytic Graphite.” Small (Weinheim an der Bergstrasse, Germany) 3.6 (2007): 1007–14.
[59]Miyake, Yusuke, Hirofumi Tanaka, and Takuji Ogawa. “Scanning Tunneling Microscopy Investigation of Vanadyl and cobalt(II) Octaethylporphyrin Self-Assembled Monolayer Arrays on Graphite.” Colloids and Surfaces A: Physicochemical and Engineering Aspects 313-314 (2008): 230–233.
[60]Scudiero, L, and K W Hipps. “Controlled Manipulation of Self-Organized Ni (II) - Octaethylporphyrin Molecules Deposited from Solution on HOPG with a Scanning Tunneling Microscope.” Ii (2007): 17516–17520.
[61]Tao, Feng. “Nanoscale Surface Chemistry in Self- and Directed-Assembly of Organic Molecules on Solid Surfaces and Synthesis of Nanostructured Organic Architectures.” Pure and Applied Chemistry 80.1 (2008): 45–57.

[62]Tao, Feng, Julie Goswami, and Steven L Bernasek. “Competition and Coadsorption of Di-Acids and Carboxylic Acid Solvents on HOPG.” The journal of physical chemistry. B 110.39 (2006): 19562–9.
[63]Qiu, Xiaohui et al. “Alkane-Assisted Adsorption and Assembly of Phthalocyanines and Porphyrins.” 12 (2000): 5550–5556.
[64]Otsuki, Joe et al. “Surface Patterning with Two-Dimensional Porphyrin Supramolecular Arrays.” Journal of the American Chemical Society 127.29 (2005): 10400–5.
[65]Otsuki, Joe et al. “Face-on and Columnar Porphyrin Assemblies at Solid/Liquid Interface on HOPG.” Chem. Lett. 38 (2009): 570-1.
[66]Nicholls, Dylan, William P Mckinzie, and Nuri Oncel. “Porphyrin Adsorption on Highly Ordered Pyrolytic Graphite.” J. Phys. Chem. C 114 (2010): 14983–14985.
[67]Nicholls, Dylan et al. “A Scanning Tunneling Microscopy Study on Self-Assembled Fe(III) Meso-Tetra(4-Carboxyphenyl) Porphyrin Chloride Chains.” Thin Solid Films 534 (2013): 308–311.
[68]Oncel, Nuri, and Steven L. Bernasek. “The Effect of Molecule-Molecule and Molecule-Substrate Interaction in the Formation of Pt-Octaethyl Porphyrin Self-Assembled Monolayers.” Applied Physics Letters 92.13 (2008): 133305.
[69]Oncel, Nuri, and Steven L Bernasek. “Ni(II)- and Vanadyloctaethylporphyrin Self-Assembled Layers Formed on Bare and 5-(octadecyloxy)isophthalic Acid Covered Graphite.” Langmuir 25.16 (2009): 9290–5.
[70]Barlow, Dan E, L Scudiero, and K W Hipps. “Scanning Tunneling Microscopy Study of the Structure and Orbital-Mediated Tunneling Spectra of cobalt(II) Phthalocyanine and cobalt(II) Tetraphenylporphyrin on au(111): Mixed Composition Films.” Langmuir 20.11 (2004): 4413–21.
[71]Lei, S. B. et al. “Surface Stabilized Porphyrin and Phthalocyanine Two-Dimensional Network Connected by Hydrogen Bonds.” The Journal of Physical Chemistry B 105.44 (2001): 10838–10841.
[72]Xu, Bo et al. “Stabilization Effect of Alkane Buffer Layer on Formation of Nanometer-Sized Metal Phthalocyanine Domains.” (2000): 10502–10505.
[73]Miura, Yoshiko et al. “Multilayer Formation of Oriented Helical Peptides Glued by Hydrogen Bonding.” Thin Solid Films 393.1-2 (2001): 59–65.
[74]Reiter, M., M. Edelwirth, W.M. Heckl and S.J. Sowerby (1999). Scanning tunneling microscopy of adenine monolayers self-assembled on the graphite surface: Molecular packing and crystallite morphology. Probe Microscopy 1:291-301.
[75]Zubavichus, Yan et al. “X-Ray Photoelectron Spectroscopy and near-Edge X-Ray Absorption Fine Structure Study of Water Adsorption on Pyridine-Terminated Thiolate Self-Assembled Monolayers.” Langmuir 20.25 (2004): 11022–9.
[76]Ogunrinde, Ayowale, K W Hipps, and L Scudiero. “A Scanning Tunneling Microscopy Study of Self-Assembled nickel(II) Octaethylporphyrin Deposited from Solutions on HOPG.” Langmuir 22.13 (2006): 5697–701.
[77]Yuan, Qunhui, Yangjun Xing, and Eric Borguet. “An STM Study of the pH Dependent Redox Activity of a Two-Dimensional Hydrogen Bonding Porphyrin Network at an Electrochemical Interface.” Journal of the American Chemical Society 132.14 (2010): 5054–60.
[78]Blake, P. et al. “Making Graphene Visible.” Applied Physics Letters 91.6 (2007): 063124.
[79]Wallace, P. R. “The Band Theory of Graphite.” Physical Review Letters 71.9 (1947): 622–634.
[80]Saito, R. et al. Physical Properties of Carbon Nanotubes. London: World Scientific Publishing Co. 1998.
[81]Riedl, C., and U. Starke. “Structural Properties of the Graphene-SiC(0001) Interface as a Key for the Preparation of Homogeneous Large-Terrace Graphene Surfaces.” Physical Review B 76.24 (2007): 245406.

[82]Starke, U, and C Riedl. “Epitaxial Graphene on SiC(0001) and SiC(000¯1): From Surface Reconstructions to Carbon Electronics.” Journal of physics. Condensed matter 21.13 (2009): 134016.
[83]Feenstra, R. M., and Shu Nie. “Tunneling Spectroscopy of Graphene and Related Reconstructions of SiC(0001).” J. Vac. Sci. and Tehnol. A 27 (2009): 1052.
[84]Choi, Junghun et al. “Chemical Doping of Epitaxial Graphene by Organic Free Radicals.” The Journal of Physical Chemistry Letters 1.2 (2010): 505–509.
[85]Lauffer, Peter et al. “Molecular and Electronic Structure of PTCDA on Bilayer Graphene on SiC(0001) Studied with Scanning Tunneling Microscopy.” Physica Status Solidi (B) 245.10 (2008): 2064–2067.
[86]Ptersson, S. et al. “Formation of iridium silicides from Ir Thin films on Si substrates.” J. Appl. Phys. 50 (1979): 3357-65.
[87]Knaepen, W. et al. “In Situ X-Ray Diffraction Study of Thin Film Ir/Si Solid State Reactions.” Microelectronic Engineering 87.3 (2010): 258–262.
[88]Nicholls, Dylan, and Nuri Oncel. “Iridium-Modified Si(111) Surface.” Journal of Physics. Condensed matter 25.44 (2013): 445004.
[89]Oncel, Nuri and Dylan Nicholls. “Iridium Silicide Nanowires on Si(001) Surfaces.” Journal of Physics. Condensed Matter 25.1 (2013): 014010.
[90]Bennett, P. A. et al. “Ring Clusters in Transition-Metal-Silicon Surface Structures.” Physical Review Letters 69.8 (1992): 1224–1227.
[91]Parikh, S. A. et al. “Transition metal induced ring-cluster structures on Si(111).” Journal of Vacuum Sci. & Tech. A 13 (1995): 1589.
[92]Odagiri, Mayu et al. “Direct Observation of Si(111) √7×√7-Co Structure and Its Local Electronic Structure.” Applied Physics Letters 97.15 (2010): 151911.
[93]Wolkow, R., and Ph. Avouris. “Atom-Resolved Surface Chemsitry Using Scanning Tunneling Microscopy.” Physical Review Letters 60.11 (1988): 1049–52.
[94]Hamers, R. J., R. M. Tromp, and J. E. Demuth. “Surface Electronic Structure of Si(111)-(7x7) Resolved in Real Space.” Physical Review Letters 56.18 (1986): 1972–75.
[95]Zandvleit, H. J. W. et al. “Energetics of Ni-Induced Vacancy Line Defects on Si(001).” Physical Review Letters 75.21 (1995): 3890–3.
[96]Zandvliet, H. “Energetics of Si(001).” Reviews of Modern Physics 72.2 (2000): 593–602.
[97]Wang, Jing, T. A. Arias, and J. D. Joannopoulos. “Dimer Vacancies and Dimer-Vacancy Complexes on the Si(100) Surface.” Physical Review B 47.16 (1993): 497–509.
[98]Chao, Kuo-jen et al. “Dimer-Vacancy-Dimer-Vacancy Interaction on the Si(001) Surface: The Nature of the 2xn Structure.” Physical Review B 52.12 (1995): 8650–8654.
[99]Zandvliet, H. J. W. “Ordering of Vacancies on Si(001).” Surface Science 377-379 (1997): 1–6.